International Journal of Impact Engineering 190 (2024) 104972

Contents lists available at ScienceDirect

International Journal of Impact Engineering

journal homepage: www.elsevier.com/locate/ijimpeng

Quasi-static and dynamic tensile behaviour of 316L stainless steels: Rolled versus laser-powder bed fusion (LPBF) fabricated samples

Jian Liu [a,b], Le Dong [a,b], Cunyi Li [c], Jianguang Fang [c,*], Ying Chen [d], Jian Cui [e]

[a] Earthquake Engineering Research and Test Center, Guangzhou University, Guangzhou 510405, PR China
[b] Key Laboratory of Earthquake Resistance, Earthquake Mitigation and Structural Safety, Ministry of Education, Guangzhou 510405, PR China
[c] School of Civil and Environmental Engineering, University of Technology Sydney, Ultimo, NSW 2007, Australia
[d] School of Mechanics and Construction Engineering, Jinan University, Guangzhou 510632, PR China
[e] School of Civil Engineering, Tianjin University, Tianjin 300072, PR China

ARTICLE INFO

Keywords:
316L stainless steel
Laser powder bed fusion (LPBF)
Dynamic tensile behaviour
Strain rate effect
Building orientation
Modified Johnson-Cook (J-C) model

ABSTRACT

This study assessed the quasi-static and dynamic tensile properties of additive manufactured 316L stainless steel through a series of direct tensile tests. The fabrication of the additive manufactured 316L stainless steel specimens was achieved through the laser powder bed fusion (LPBF) technique, with specimens prepared in various building orientations. For comparison, traditional rolled 316L stainless steel was also tested in various rolling orientations. The influences of the strain rate and rolling/building orientations on the tensile behaviour of rolled and LBPF printed 316L stainless steels were investigated. Fracture morphology and mode were also observed using the scanning electron microscopy (SEM) technique. Furthermore, experimental data was fitted by the Cowper-Symonds model to determine the strain rate effects on the material yield and ultimate strengths. To describe the quasi-static and dynamic tensile behaviours of the rolled and LBPF printed 316L stainless steels, a modified Johnson-Cook (J-C) model incorporating the Voce hardening model and considering the strain rate effect was employed.

1. Introduction

Additive manufacturing, also referred to as three-dimensional (3D) printing, is a rapid prototyping technology that uses digital models to create highly dense microstructures through layer-by-layer deposition of adhesive materials, including polymer, ceramic, resin, metal wire and powder, etc. [1–7]. In comparison to the traditional rolling or casting techniques, additive manufacturing offer advantages in metal fabrication such as efficient metallic material utilisation, streamlined manufacturing processes and potential for improved material properties [8–10]. Moreover, this technology enables a one-step formation of metallic structures in a specific direction, eliminating the need for welding treatment at weak junction points and enhancing overall structural integrity. With these advantages, additive manufacturing technology helps produce large-scale and high-strength metallic structures featuring complex geometric shapes and internal configurations, making it highly promising for widespread applications in automotive, aerospace and protective engineering. With the significant advancements in the application of additive manufacturing for metallic materials in recent years [11–14], mainstream printing methods encompass material extrusion (MEX), binder jetting (BJT), material jetting (MJT), sheet lamination (SHL), vat photopolymerization (VPP), directed energy deposition (DED), and powder bed fusion (PBF) [15,16]. Representative techniques within the PBF method include selective laser sintering (SLS), electron beam melting (EBM), laser powder bed fusion (LPBF) (or selective laser melting (SLM)), among others. LPBF, which was originated in the 1990s [17], has emerged as a widely employed additive manufacturing technique. Its popularity stems from the ability to flexibly adjust process parameters, such as the laser power, scanning speed and spacing, enabling the production of intricate geometric structures with exceptional precision and surface quality.

316L stainless steel is a low-carbon alloy known for its corrosion resistance, good toughness and cost-effectiveness. The additive manufactured 316L stainless steel can be applied to aircraft landing gear, automotive components or protective structures. However, these structures are susceptible to impact and blast loads during their service life or extremely hazardous conditions. Alongside investigations into the quasi-static macroscopic mechanical properties [18,19], surface state [20],

* Corresponding author.
E-mail addresses: jian.liu@gzhu.edu.cn (J. Liu), jianguang.fang@uts.edu.au (J. Fang).

https://doi.org/10.1016/j.ijimpeng.2024.104972
Received 30 October 2023; Received in revised form 7 March 2024; Accepted 6 April 2024
Available online 16 April 2024

microstructure [21], laser process parameters [22] and microscale modelling [23], significant research efforts have been dedicated to exploring the dynamic compressive behaviour of additive manufactured 316L stainless steel at high strain rates more than 1000 s^{-1} [24–29]. The dynamic response and failure of laser additive manufacturing 316L stainless steel exhibit a complex process, influenced by a combination of macroscopic behaviours including strain hardening, adiabatic shear localisation, as well as microscopic behaviours such as dislocation slip and dynamic recrystallization.

However, studies focusing on its dynamic tensile behaviour, particularly under the strain rate less than 1000 s^{-1} (intermediate and high strain rate levels [30]), still remain limited. Khodabakhshi et al. [31] contrasted the dynamic tensile performance of laser additive manufactured 316L stainless steel with conventional commercial 316L stainless steel, covering a strain rate spectrum of 1 s^{-1}. The research outcomes highlighted that the strain rate minimally affected the tensile flow stress, while the fracture strain of conventional 316L stainless steel notably exceeded that of the additive manufactured counterpart. Within a low strain rate range of 0.1 s^{-1}, Li et al. [32] studied the tensile performance of LPBF printed 316L stainless steel, observing increased yield strength with higher strain rates alongside reduced ductility. Jiang et al. [33] delved into the dynamic tensile behaviour of SLM printed 316L stainless steel at a low strain rate range of 0.22 s^{-1}. They noted a decrease in both the strain hardening coefficient and fracture strain as the strain rate increased, with the flow stress exhibiting positive strain rate sensitivity. Tancogne-Dejean et al. [34] examined the dynamic tensile behaviour of BJT printed 316L stainless steel within a strain rate range of 160 s^{-1}. Their findings indicated an improvement of the flow stress with the strain rate, without evident variations in the hardening rate. Carassus et al. [35] assessed the dynamic tensile performance of SLM printed 316L stainless steel with three various thicknesses of 0.5 mm, 0.75 mm and 1 mm within a strain rate range of 1000 s^{-1}. The experimental results suggested a minimum specimen thickness exceeding 0.75 mm to fulfil test requirements due to weaker inter-layers. Li et al. [27] conducted dynamic tensile tests and observed a positive strain rate effect on the initial yield stress, whereas the strain hardening appeared rate-independent within a strain rate range of 1000 s^{-1}.

The anisotropic behaviour of additive manufactured metal materials is a significant concern, as different building orientations can result in non-negligible disparities in material response based on the loading direction. Most current research on the anisotropic behaviour of additive manufactured metal materials primarily focuses on the quasi-static conditions. Güden et al. [36] assessed the mechanical properties of SLM printed 316L stainless steel with various inclination angles relative to the building direction (0°, 15°, 30°, 45°, 60°, 75° and 90°). The experimental results showed that, as the inclination angle increased, both yield strength and tensile strength increased, but ductility decreased. Li et al. [27] also found that increasing the inclination angle led to higher strength but reduced toughness. Carroll et al. [37] studied the tensile behaviour of DED printed Ti–6Al–4V alloy in both longitudinal and transverse building orientations through macroscopic mechanical tests and microscale observations. It was revealed that transversely oriented specimens exhibited superior toughness. Ni et al. [38] explored the microstructure and mechanical properties of SLM printed chromium-nickel-iron alloy 718. The test results indicated excellent tensile strength in specimens produced in both longitudinal and transverse directions, primarily because of the high cooling rate during laser processing, resulting in a refined microstructure, while the strength and ductility anisotropy were influenced by the columnar grain morphology. Niendorf et al. [39] also observed anisotropy in SLM printed 316L stainless steel depending on the building direction, resulting in varying grain sizes and preferred textures. Researchers have shown interests in investigating the dynamic compressive response of additive manufactured metals with varying building orientations. Alaghmandfard et al. [40] explored the dynamic compressive properties of Ti–6Al–4V alloy printed adopting the EBM technique in both vertical and horizontal orientations within a strain rate range of 1100 s^{-1}. The research outcomes demonstrated that, under the same compressive strain rate, vertically printed specimens displayed higher impact strength. This was explained by the nearly parallel alignment of prior β-grain boundaries with the impact direction and grain boundary strengthening. Yuan et al. [41] comparatively analysed the dynamic compressive behaviour of Ti–6Al–4V alloy SLM printed along the building, diagonal and transverse directions within a strain rate range of 4593 s^{-1}. The findings highlighted the building orientation-dependent dynamic mechanical properties of additive manufactured Ti–6Al–4V alloy, revealing significant positive strain rate sensitivity in terms of the material strength.

The current study aims to explore the influences resulting from strain rates and building orientations on the quasi-static and dynamic tensile responses of LPBF printed 316L stainless steel within the strain rate range of 535.28 s^{-1}. Additionally, a comparative assessment is conducted on the tensile properties between the traditional rolled and LPBF printed 316L stainless steels. Their fracture morphology and mode are further elucidated through the scanning electron microscopy (SEM) observations. Utilising the test data, the Cowper-Symonds model is calibrated to determine the strain rate effect on the yield and ultimate strengths of both rolled and LPBF printed 316L stainless steels. Further, a modified Johnson-Cook (J-C) constitutive model that integrates the Voce hardening model and considers the strain rate effect is employed to characterise their quasi-static and dynamic tensile behaviours.

2. Testing specimen preparation

Table 1 presents the chemical components of rolled 316L stainless steel (TR-316L) and LPBF printed 316L stainless steel (LPBF-316L) utilised in the current study. The TR-316L specimens were prepared by the Electrical Discharge Machining (EDM) wire cutting technique. All the LPBF-316L specimens were fabricated in the laboratory of Suzhou XDM 3D Printing Technology Limited Company in Jiangsu Province, using the EOS M290 system (EOS GmbH, Krailing, Germany) with a scanning strategy featuring 67° inter-layer rotation. The argon gas was adopted as a protective atmosphere to prevent the molten metal from reacting with the oxygen. To minimise residual stresses generated from the high-temperature melting, all the specimens underwent post-heat treatment in a furnace, with a heating rate of 6.5 °C/min from room temperature to 400 °C for 4 h, and then cooled to room temperature at a rate of 1 °C/min. The LPBF printing parameters applied in the current study are outlined in Table 2.

To explore the anisotropic behaviour of TR-316L and LPBF-316L under quasi-static and dynamic tensile loads, specimens were prepared with various orientations, as illustrated in Fig. 1. TR-316L and LPBF-316L sheets were firstly fabricated in the vertical orientation. In terms of the quasi-static tensile tests, the TR-316L specimens were prepared with three inclination angles relative to the rolling orientation, including 0° rolling direction (RD), 45° diagonal direction (DD) and 90° transverse direction (TD). Similarly, the LPBF-316L specimens were established with three inclination angles relative to the building orientation, encompassing 0° building direction (BD), 45° DD and 90° normal direction (ND). Regarding the dynamic tensile tests, the TR-316L specimens were established along RD, DD and TD, while the LPBF-316L specimens were built along BD and ND. In each testing scenario, a minimum of two identical specimens were prepared for experimentation to guarantee the reliability of the test results.

TR-316L and LPBF-316L specimens shared the identical planar geometry in each batch of tests for comparative analysis. For the quasi-static tensile tests, the geometric dimensions of the specimens are illustrated in Fig. 2**(a)**, wherein the specimens possessed a gauge length of 20 mm, a width of 10 mm and an overall length of 100 mm, and the clamping ends are transitioned through the arcs with a radius of 10 mm. To satisfy the testing requirements in the dynamic tensile tests, adjustments were made to the clamping lengths of the specimens, as depicted in Fig. 2**(b)**, from which the lower and upper clamping ends were

Table 1
Chemical components of TR-316L and LPBF-316L (%).

	Cr	Ni	Mo	Mn	Si	C	P	S	N
TR-316L	16.9	10	2.03	0.91	0.53	0.022	0.03	< 0.01	0.031
LPBF-316L	16.6	10.1	2.15	1.06	0.5	< 0.03	< 0.045	< 0.03	/

Table 2
Printing parameters in the LPBF technique.

Laser power	Laser scanning rate	Layer thickness	Hatch spacing	Powder particle size
280 W	1200 mm/s	30 μm	0.14 mm	15–60 μm

extended to 45 mm and 230 mm, respectively. These adjustments allow the specimen loaded with a constant rate, requiring a longer acceleration time to ensure stress equilibrium [42,43]. The gauge length of the specimens in the dynamic tensile tests remained consistent with that in the quasi-static1 tensile tests. The thickness of the TR-316L specimens in both quasi-static and dynamic tensile tests was fixed at 1.4 mm, while the thicknesses of the LPBF-316L specimens in the quasi-static and dynamic tensile tests were respectively set to 1.68 mm and 1.5 mm.

3. Testing facilities and setup

The INSTRON 3369 hydraulic testing machine with a loading capacity of 50 kN and a testing rate range of 0.1–500 mm/min was utilised for the quasi-static tensile tests. The loading rate was configured at 5 ×

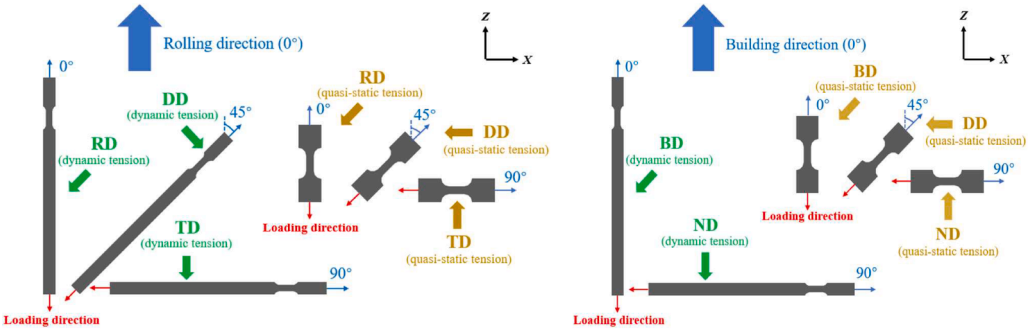

(a) TR-316L (b) LPBF-316L

Fig. 1. Rolling/building directions of TR-316L and LPBF-316L specimens.

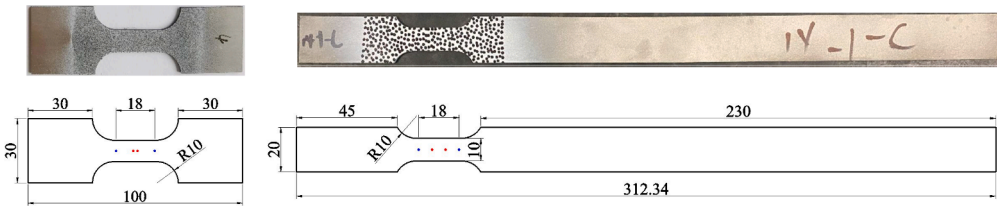

(a) Quasi-static tension (b) Dynamic tension

Fig. 2. The geometric dimensions of TR-316L and LPBF-316L specimens in quasi-static and dynamic tensile tests (unit: mm).

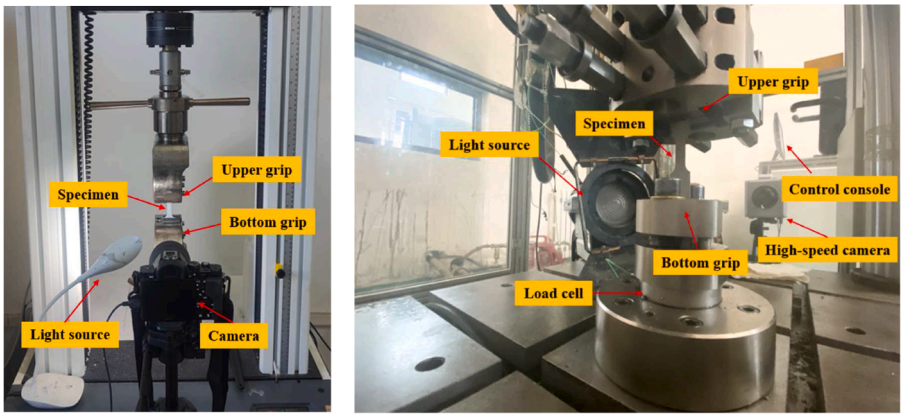

(a) Quasi-static tensile test (b) Dynamic tensile test

Fig. 3. Experimental setup of quasi-static and dynamic tensile tests on TR-316 L and LPBF-316 L specimens.

10^{-5} m/s. Prior to testing, the gauge length region was cleaned and then coated with the white paint. Following the drying process, uniform and randomly distributed black speckles were sprayed onto the white paint surface. A camera was employed to capture the complete displacement evolution of the specimen, wherein the camera frame rate was set at 50 frames per second (fps). The experimental setup of the quasi-static tensile test is depicted in Fig. 3(a). Then, dynamic tensile tests were performed with the utilisation of the high-speed servo-controlled hydraulic testing machine, namely INSTRON VHS 160/100–20, which has a loading capacity of 100 kN and a testing rate range of 0.1–20 m/s. Six different loading rates, including 0.03 m/s, 0.3 m/s, 1 m/s, 4 m/s, 8 m/s and 14 m/s, were performed. These loading rates corresponded to the strain rates of 1.5 s^{-1}, 15 s^{-1}, 50 s^{-1}, 200 s^{-1}, 400 s^{-1} and 700 s^{-1}, respectively. To record the damage progression and measure the strain of the specimens, a high-speed camera was located in front of the testing machine using the Digital Image Correlation (DIC) technology. In terms of the aforementioned loading rates, a variety of frame rates (reaching up to 120,000 fps) for the high-speed camera were adopted, which could allow for both accurate capturing of speckle deformation and reduced computational costs during post-software processing. The experimental setup of the dynamic tensile test is illustrated in Fig. 3(b). Table 3 lists the quasi-static and dynamic tensile test plan for the TR-316L and LPBF-316L specimens with different rolling/building directions and loading rates.

4. Tensile testing results

4.1. Determination of strain rate

The nominal strain rate ($\dot{\varepsilon}_n$) can be defined by the following equation:

$$\dot{\varepsilon}_n = v/l \tag{1}$$

where v denotes the loading rate; l denotes the gauge length. The strain rate is non-uniform especially under high tensile loading conditions, primarily owing to the generation of uneven stress amplitudes within the specimen during the initial stages [42,44,45]. Therefore, accurately determining the true strain rate of metallic materials is of great significance to characterise their dynamic behaviour. It was also found from the previous studies [42,46] that, owing to the influence of stress waves, there is a disparity between the theoretical and true strain rates. Thus, a linear fitting approach was employed to determine the strain rate from the strain-time curves of TR-316L and LPBF-316L specimens under tensile loadings. Fig. 4 presents a typical example of fitting true strain rates for LPBF-316L-ND under dynamic tensile loads on the basis of the strain-time curves.

Table 3
Quasi-static and dynamic tensile test plan for TR-316L and LPBF-316L specimens.

Tensile test	Specimen	Fabrication method	Rolling/building direction	Loading rate (m/s)
Quasi-static	TR-316L-RD	TR	RD	5×10^{-5}
	TR-316L-DD	TR	DD	5×10^{-5}
	TR-316L-TD	TR	TD	5×10^{-5}
	LPBF-316L-BD	LPBF	BD	5×10^{-5}
	LPBF-316L-DD	LPBF	DD	5×10^{-5}
	LPBF-316L-ND	LPBF	ND	5×10^{-5}
Dynamic	TR-316L-RD	TR	RD	0.03, 0.3, 1, 4, 8, 14
	TR-316L-DD	TR	DD	0.03, 0.3, 1, 4, 8, 14
	TR-316L-TD	TR	TD	0.03, 0.3, 1, 4, 8, 14
	LPBF-316L-BD	LPBF	BD	0.3, 1, 4, 8
	LPBF-316L-ND	LPBF	ND	0.3, 1, 4, 8, 14

4.2. Quasi-static tensile test

Table 4 presents the average quasi-static tensile test results of the TR-316L and LPBF-316L specimens with various rolling/building directions. The corresponding quasi-static engineering tensile stress-strain curves are depicted in Fig. 5**(a)**. It was found that both TR-316L and LPBF-316L specimens displayed evident elasticity prior to yielding. The TR-316L specimens exhibited a less variance in the yield and ultimate strengths as compared to the LPBF-316L specimens along three various building directions. However, a notable discrepancy was observed in the ductility of the TR-316L specimens, with TR-316L-TD demonstrating considerably lower fracture strain compared to TR-316L-RD and TR-316L-DD. The LPBF-316L specimens exhibited a notable rise in both yield and ultimate strengths when increasing the inclination angle relative to the building direction, accompanied by a reduction in the ductility. These phenomena were consistent with the findings as reported by Güden et al. [36] and Li et al. [27], indicating that quasi-static tensile behaviour of the LPBF-316L specimens was evidently affected by the building direction. Fig. 5**(b)** displays the strain hardening and quasi-static true tensile stress-strain curves for the TR-316L and LPBF-316L specimens, wherein the true stress (σ_t) and strain (ε_t) were respectively derived from the equations as follows:

$$\sigma_t = \sigma_e(1 + \varepsilon_e) \tag{2}$$

$$\varepsilon_t = \ln(1 + \varepsilon_e) \tag{3}$$

where σ_e and ε_e represent the engineering stress and strain, respectively. The strain hardening-true strain curves for both TR-316L and LPBF-316L specimens could be divided into three stages [26,47]. Taking TR-316L-DD and LPBF-316L-DD as examples, there was a rapid decrease until a strain of 0.038 (Stage I), followed by a slower decrease within the strain range of 0.038–0.356 (Stage II) and another rapid decrease when the strain exceeds 0.356 (Stage III). Also noted in Fig. 5**(b)**, the strain hardening of the TR-316L specimens prepared from different rolling directions, i.e. TR-316L-RD, TR-316L-DD and TR-316L-TD, was nearly identical and significantly higher than those of the LPBF-316L specimens along three various building directions. This revealed that LPBF-316L

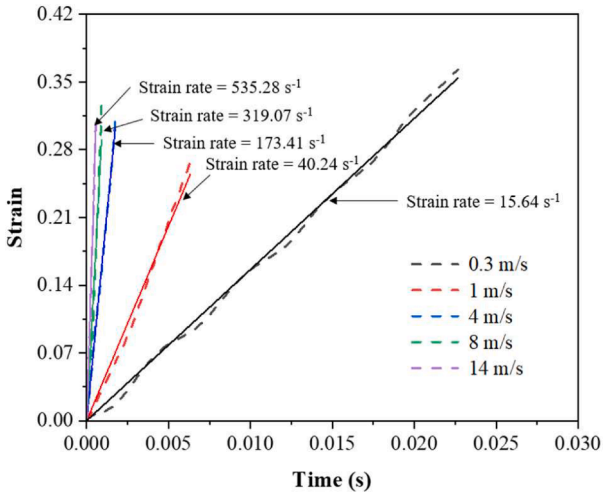

Fig. 4. An example of fitting true strain rates for LPBF-316L-ND under dynamic tensile loads from the strain-time curves.

Table 4
Quasi-static tensile test results of TR-316L and LPBF-316L specimens.

Specimen	Strain rate (s^{-1})	Yield strength (MPa)	Ultimate strength (MPa)	Engineering fracture strain
TR-316L-RD	0.0018 ± 1E-4	284.89 ± 2.09	638.74 ± 0.59	0.608 ± 0.017
TR-316L-DD	0.0018 ± 1E-4	280.35 ± 2.76	618.01 ± 3.37	0.61 ± 0.024
TR-316L-TD	0.0016 ± 1E-4	285.76 ± 3.31	632.83 ± 5.75	0.507 ± 0.038
LPBF-316L-BD	0.0019 ± 1E-4	510.51 ± 1.12	648.52 ± 0.17	0.613 ± 0.015
LPBF-316L-DD	0.0025 ± 1E-4	515.68 ± 0.71	668.36 ± 1.18	0.581 ± 0.001
LPBF-316L-ND	0.0028 ± 3E-4	532.80 ± 1.83	702.97 ± 1.32	0.514 ± 0.013

had a weaker hardening effect throughout the deformation process as compared to TR-316L, whereas it could maintain higher stress. When comparing the LPBF-316L specimens prepared along three various building directions within the strain range of approximately 0.018 to 0.186, LPBF-316L-ND exhibited the highest strain hardening rate, followed by LPBF-316L-DD and LPBF-316L-BD.

4.3. Dynamic tensile test

As a result of the rapid loading applied during dynamic tensile tests, stress waves would be generated within the specimen and potentially lead to specimen fracture before reaching dynamic stress equilibrium. In the pursuit of attaining dynamic stress equilibrium, stress waves require sufficient time to propagate back and forth within the specimen, typically spanning at least three cycles [48]. The velocity of the stress wave propagation (c_s) within the specimen could be determined by:

$$c_s = \sqrt{E/\rho} \tag{4}$$

where E and ρ denote the material elastic modulus and density, respectively. The elastic moduli for TR-316L, LPBF-316L-BD, LPBF-316L-DD and LPBF-316L-ND 316L were calculated as 167 GPa, 145 GPa, 153 GPa and 166 GPa, respectively. The density for both TR-316L and LPBF-316L specimens was fixed at 7900 kg/m^3. For conservative purpose, LPBF-316L-ND at the strain rate of 535.28 s^{-1}, as shown in Fig. 4, was taken as a critical example to validate the dynamic stress equilibrium. Correspondingly, c_s was calculated to be 4284 m/s, and the time required for one round-trip was estimated to be 0.0093 ms. LPBF-316L-ND at 535.28 s^{-1} fractured at 0.5568 ms, enabling the stress waves to complete more than 50 round-trips, thereby confirming the dynamic stress equilibrium.

It is important to highlight that, due to the inevitable oscillation during dynamic loading, the stress-strain curves of the TR-316L and LPBF-316L specimens in the dynamic tensile tests were filtered and smoothed using the adjacent averaging method [30], alongside additional measures like threshold selection, manual inspection and utilisation of neighbouring data points for ensuring the reliability of the dynamic yield stress. Also noted, in cases where the linear elastic region was highly unreliable under dynamic loads, the approach proposed by Sun et al. [49] was adopted to determine the dynamic yield stress. This method, assuming the minimal strain rate effect on the elastic modulus, involved offsetting the line representing the quasi-static elastic modulus by 0.2%, after which the hardening portion of the engineering stress-strain curve was fitted with a straight line. The intersection of these two lines corresponded to the dynamic yield stress, as illustrated in Fig. 6.

Table 5 provides the average dynamic tensile test results on the TR-316L and LPBF-316L specimens from various rolling/building directions. The dynamic increase factor (DIF), which is defined as the ratio of material dynamic strength (f_d) to static strength (f_s), serves as a crucial index for measuring material mechanical sensitivity and has reported as a function of strain rate [50], thus the DIF values of the yield strength (DIF_y) and ultimate strength (DIF_u) for the TR-316L and LPBF-316L specimens were subsequently calculated and present in Table 5. Fig. 7 depicts the dynamic engineering tensile stress-strain curves of the TR-316L and LPBF-316L specimens. Both TR-316L and LPBF-316L specimens demonstrated substantial positive sensitivity to the strain rate in terms of the yield and ultimate strengths. Also noted, the engineering fracture strain of the TR-316L and LPBF-316L specimens was affected by the strain rate, wherein the TR-316L specimens, particularly for TR-316L-RD and TR-316L-DD, and LPBF-316L specimens, including LPBF-316L-BD and LPBF-316L-ND, under the

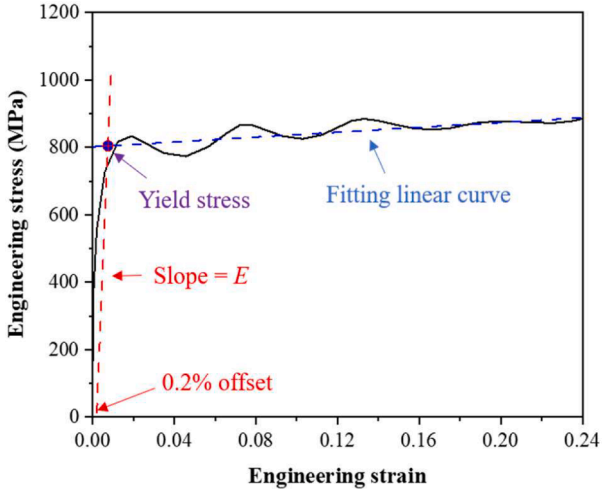

Fig. 6. Determination of dynamic yield stress.

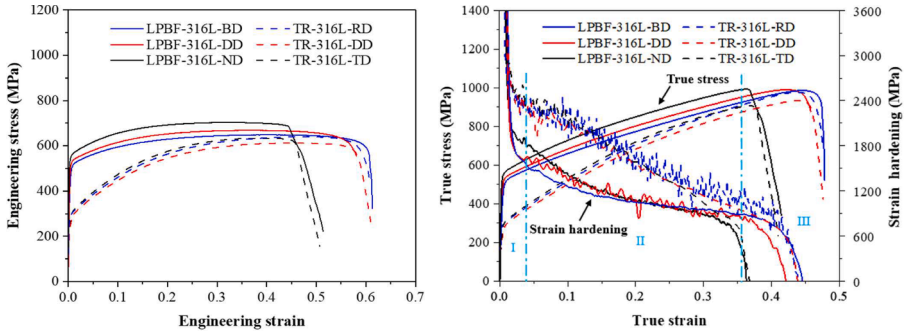

(a) Engineering stress-strain curves (b) True stress-strain curves

Fig. 5. Quasi-static tensile stress-strain curves of TR-316L and LPBF-316L specimens with various rolling/building directions.

Table 5
Dynamic tensile test results of TR-316L and LPBF-316L specimens.

Specimen	Tensile loading rate (m/s)	Strain rate (s^{-1})	Yield strength (MPa)	Ultimate strength (MPa)	Engineering fracture strain	DIF_y	DIF_u
TR-316L-RD	0.03	0.88 ± 0.03	356.32 ± 4.74	664.15 ± 8.93	0.51 ± 0.01	1.25 ± 0.017	1.04 ± 0.014
	0.3	9.22 ± 0.06	367.97 ± 7.38	687.45 ± 6.02	0.53 ± 0.01	1.29 ± 0.026	1.08 ± 0.009
	1	33.32 ± 1.75	429.05 ± 14.03	714.43 ± 1.01	0.54 ± 0.01	1.51 ± 0.049	1.12 ± 0.002
	4	130.32 ± 5.84	437.19 ± 9.28	722.36 ± 10.11	0.55 ± 0.01	1.51 ± 0.033	1.13 ± 0.016
	8	250.7 ± 11.55	485.57 ± 33.31	741.79 ± 15.65	0.57 ± 0.01	1.51 ± 0.12	1.16 ± 0.025
	14	433.68 ± 2.89	490.18 ± 28.20	767.53 ± 30.93	0.58 ± 0.02	1.7 ± 0.099	1.2 ± 0.048
TR-316L-DD	0.03	0.88 ± 0.05	360.86 ± 5.67	669.86 ± 10.65	0.52 ± 0.01	1.29 ± 0.02	1.08 ± 0.017
	0.3	8.69 ± 0.11	376.07 ± 4.01	679.56 ± 8.07	0.53 ± 0.01	1.34 ± 0.014	1.1 ± 0.013
	1	33.01 ± 1.72	416.85 ± 11.72	710.46 ± 4.03	0.53 ± 0.01	1.49 ± 0.042	1.15 ± 0.007
	4	123.89 ± 1.87	447.48 ± 18.92	728.76 ± 3.88	0.55 ± 0.01	1.6 ± 0.067	1.18 ± 0.006
	8	246.41 ± 7.91	487.12 ± 13.67	733.5 ± 15.65	0.57 ± 0.01	1.74 ± 0.049	1.19 ± 0.025
	14	434.52 ± 5.73	497.06 ± 15.57	751.73 ± 20.64	0.58 ± 0.02	1.77 ± 0.056	1.22 ± 0.033
TR-316L-TD	0.03	0.88 ± 0.02	364.13 ± 7.74	664.66 ± 3.51	0.52 ± 0.01	1.27 ± 0.027	1.05 ± 0.006
	0.3	7.94 ± 0.03	367.13 ± 6.95	666.67 ± 0.38	0.52 ± 0.01	1.28 ± 0.024	1.05 ± 0.001
	1	33.26 ± 0.55	417.18 ± 11.29	710.94 ± 1.24	0.55 ± 0.01	1.46 ± 0.04	1.12 ± 0.002
	4	121.44 ± 10.73	440.71 ± 13.7	738.19 ± 11.36	0.54 ± 0.02	1.54 ± 0.048	1.17 ± 0.018
	8	233.07 ± 5.15	498.01 ± 18.06	734.93 ± 10.63	0.57 ± 0.01	1.74 ± 0.063	1.16 ± 0.017
	14	432.43 ± 8.26	505.79 ± 10.63	736.18 ± 24.52	0.58 ± 0.01	1.77 ± 0.037	1.16 ± 0.039
LPBF-316L-BD	0.3	13.99 ± 0.56	679.81 ± 7.75	752.56 ± 3.89	0.41 ± 0.01	1.33 ± 0.015	1.16 ± 0.006
	1	51.29 ± 4.95	690.88 ± 14.27	769.14 ± 8.86	0.43 ± 0.03	1.35 ± 0.028	1.19 ± 0.014
	4	186.19 ± 4.48	706.92 ± 44.28	799.47 ± 16.78	0.45 ± 0.01	1.38 ± 0.087	1.23 ± 0.026
	8	328.44 ± 3.26	739.81 ± 48.71	851.13 ± 25.62	0.41 ± 0.02	1.45 ± 0.095	1.31 ± 0.04
LPBF-316L-ND	0.3	15.64 ± 1.72	726.33 ± 5.03	811.81 ± 16.8	0.34 ± 0.03	1.36 ± 0.01	1.15 ± 0.024
	1	41.05 ± 0.81	751.3 ± 12.76	851.83 ± 10.28	0.28 ± 0.02	1.41 ± 0.024	1.21 ± 0.015

(*continued on next page*)

Table 5 (*continued*)

Specimen	Tensile loading rate (m/s)	Strain rate (s^{-1})	Yield strength (MPa)	Ultimate strength (MPa)	Engineering fracture strain	DIF_y	DIF_u
	4	173.41 ± 6.41	758.72 ± 14.48	882.03 ± 12.01	0.33 ± 0.01	1.42 ± 0.027 ±	1.25 ± 0.017 ±
	8	319.07 ± 20.99	780.4 ± 35.64	918.41 ± 26.63	0.33 ± 0.04	1.46 ± 0.067 ±	1.31 ± 0.038 ±
	14	535.28 ± 3.98	815.44 ± 64.85	981.02 ± 45.1	0.31 ± 0.01	1.53 ± 0.12 ±	1.4 ± 0.064 ±

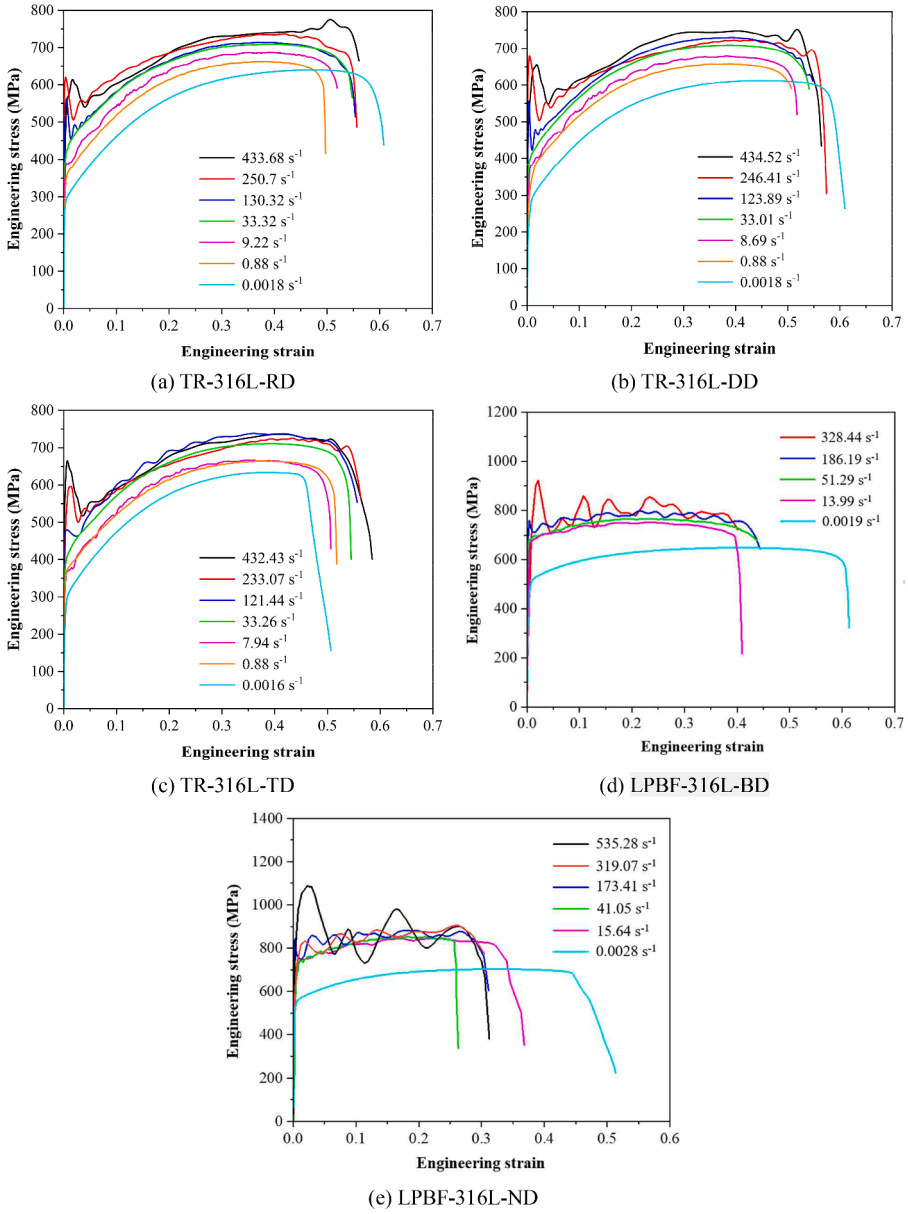

Fig. 7. Dynamic engineering tensile stress-strain curves of TR-316L and LPBF-316L specimens.

quasi-static tension exhibited the greater engineering fracture strain in comparison with the dynamic tension.

4.4. Analysis and discussions

4.4.1. Strain rate effect on material strength

Fig. 8**(a)** and **8(b)** respectively present the dynamic yield and ultimate strengths of the TR-316L and LPBF-316L specimens under various strain rates. It was evident that, under the similar strain rate, there were no significant differences in the dynamic yield and ultimate strengths among TR-316L-RD, TR-316L-DD and TR-316L-TD. Therefore, combined with the conclusion drawn from the quasi-static testing scenario, TR-316L could be considered an isotropic material in terms of the material strength. On the contrary, the LPBF-316L specimens displayed

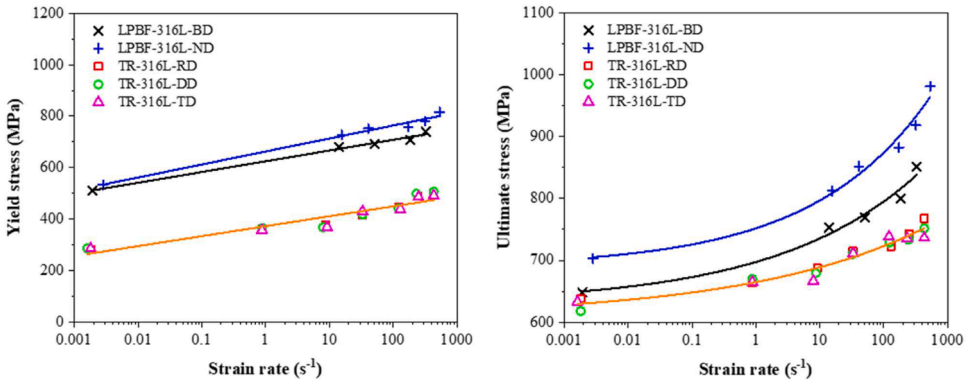

(a) Yield strength (b) Ultimate strength

Fig. 8. Dynamic yield and ultimate strengths of TR-316L, LPBF-316L-BD and LPBF-316L-ND versus strain rate.

clear anisotropic characteristics concerning the material strength, with LPBF-316L-ND consistently demonstrating higher yield and ultimate strengths in comparison with LPBF-316L-BD. In the light of the test data, empirical equations were further established to predict the yield and ultimate strengths of TR-316L, LPBF-316L-BD and LPBF-316L-ND under a variety of strain rates, which are given by:

For TR-316L:

$$f_y = 38.67\log(\dot{\varepsilon}) + 371.98,\ 0.0016\ \text{s}^{-1} < \dot{\varepsilon} < 434.52\ \text{s}^{-1} \quad (5a)$$

$$f_u = 608.87 + 55.92\exp[0.15\log(\dot{\varepsilon})],\ 0.0016\ \text{s}^{-1} < \dot{\varepsilon} < 434.52\ \text{s}^{-1} \quad (5b)$$

For LPBF-316L-BD:

$$f_y = 41.68\log(\dot{\varepsilon}) + 624.56,\ 0.0019\ \text{s}^{-1} < \dot{\varepsilon} < 328.44\ \text{s}^{-1} \quad (6a)$$

$$f_u = 629.85 + 67.48\exp[0.19\log(\dot{\varepsilon})],\ 0.0019\ \text{s}^{-1} < \dot{\varepsilon} < 328.44\ \text{s}^{-1} \quad (6b)$$

For LPBF-316L-ND:

$$f_y = 50.23\log(\dot{\varepsilon}) + 662.44,\ 0.0028\ \text{s}^{-1} < \dot{\varepsilon} < 535.28\ \text{s}^{-1} \quad (7a)$$

$$f_u = 689.56 + 62.17\exp[0.24\log(\dot{\varepsilon})],\ 0.0028\ \text{s}^{-1} < \dot{\varepsilon} < 535.28\ \text{s}^{-1} \quad (7b)$$

where f_y and f_u respectively denote the yield and ultimate strengths in the unit of 'MPa'; $\dot{\varepsilon}$ denotes the instantaneous strain rate in the unit of 's^{-1}'.

Observed from Table 5, both the TR-316L and LPBF-316L specimens exhibited the greater value of DIF_y than that of DIF_u under the similar strain rate, demonstrating that the yield strength of TR-316L and LPBF-316L was more sensitive to the strain rate than the ultimate strength. Fig. 9 illustrates DIF_y and DIF_u for the TR-316L and LPBF-316L specimens versus the strain rate. The TR-316L specimens displayed a noticeably higher sensitivity to strain rate in terms of the yield strength in comparison with the LPBF-316L specimens, whereas their sensitivity to strain rate in the ultimate tensile strength was slightly lower than that of the LPBF-316L specimens. Also noted, although evident influences resulting from the building direction on the dynamic yield and ultimate strengths of LPBF-316L specimens were observed, it was evident that DIF_y and DIF_u for LPBF-316L-BD and LPBF-316L-ND remained similar across a variety of strain rates. This phenomenon indicated that the DIF values of LPBF-316L were insensitive to the loading orientation. In other words, the strain rate sensitivity of material strengths for LPBF-316L was orientation independent.

In order to predict DIF_y and DIF_u for steel, Malvar and Crawford [51] proposed a series of empirical equations on the basis of extensive experimental data, which are expressed as follows:

$$\text{DIF} = f_d/f_s = \left(\dot{\varepsilon}/10^{-4}\right)^{\alpha*} \quad (8)$$

For the yield strength of steel, $\alpha* = 0.074 - 0.04\frac{f_y}{414}$; For the ultimate strength of steel, $\alpha* = 0.019 - 0.009\frac{f_y}{414}$. The proposed empirical equations are applicable to steel with the yield strength varying from 290 MPa to 710 MPa and the strain rate between 10^{-4} s^{-1} and 225 s^{-1}. The comparison between the test and empirically predicted outcomes of DIF values versus strain rate is illustrated in Fig. 9. Notably, the empirical equations as proposed by Malvar and Crawford tended to overestimate DIF_y for TR-316L and underestimated DIF_u for LPBF-316L. The Cowper-Symonds model [52] has been commonly employed to describe the strain rate-dependent behaviour of metallic materials [53–55]. This model scales the yield stress with the factor, as expressed by:

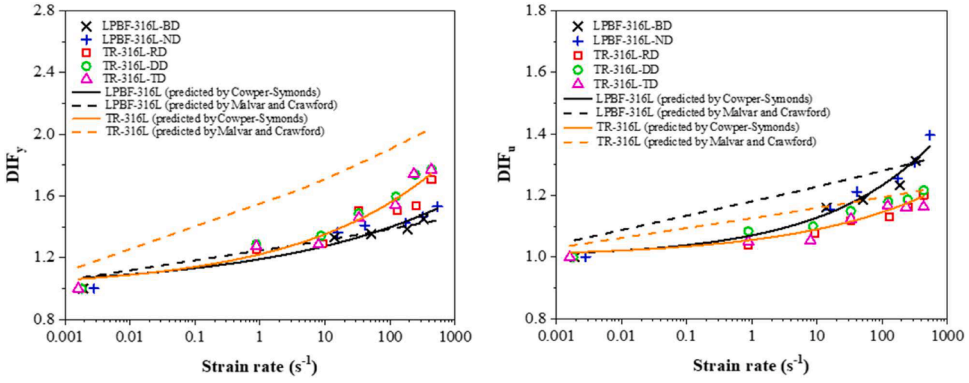

(a) DIF for yield strength (b) DIF for ultimate strength

Fig. 9. DIF values for yield and ultimate strengths of TR-316L and LPBF-316L versus strain rate.

$$\mathrm{DIF} = 1 + (\dot{\varepsilon}/C)^{1/P} \tag{9}$$

where C and P denote the strain rate parameters. In the light of the test data as presented in Fig. 9, C and P were determined using the Cowper-Symonds model for fitting the yield and ultimate strengths of TR-316L and LPBF-316L, which are listed in Table 6.

4.4.2. Strain rate effect on fracture strain

Fig. 10 and Fig. 11 depict the true strain contours obtained from the DIC technology for TR-316-RD and LPBF-316L-BD subjected to quasi-static tension and dynamic tension (at a loading rate of 8 m/s), respectively. In the case of the quasi-static tension, both TR-316-RD and LPBF-316L-BD displayed prominent necking phenomena before fracture. Excessive deformation was concentrated within the necking region, with the deformation becoming more pronounced closer to the centre of the gauge length. However, at a tensile loading rate of 8 m/s, both TR-316-RD and LPBF-316L-BD exhibited less evident necking phenomena before fracture, and the maximum true strain observed in the dynamic tension was lower than that observed in the quasi-static tension.

It is important to highlight that Fig. 5 and Fig. 7 utilised the engineering tensile stress-strain curves, which were obtained based on the gauge length of 18 mm (as illustrated by the blue dots in Fig. 2). The decision to employ engineering stress-strain curves as the material parameter was motivated by the complex stress state resulting from the necking phenomenon [46,56]. It is worth noting that, since the fracture typically occurs in the localised region, the engineering fracture strain tends to underestimate the actual fracture strain. For the sake of analysis and comparison, as well as considering the speckle quality and camera resolution, the actual fracture strains of the LPBF-316L and TR-316L specimens were determined by employing the gauge lengths of 2 mm and 6 mm (as indicated by the red dots in Fig. 2) under quasi-static and dynamic tensile tests, respectively, which are shown in Fig. 12. It was revealed that under the similar dynamic tensile loading conditions, the LPBF-316L specimens exhibited smaller fracture strains than the TR-316L specimens. Regarding the dynamic tension, the rolling/loading orientation had a limited impact on the fracture strain of the TR-316L specimens. However, the orientation sensitivity was more evident in the case of the LPBF-316L specimens, with LPBF-316L-BD exhibiting a higher fracture strain than LPBF-316L-ND. Both the LPBF-316L and TR-316L specimens displayed higher fracture strains under the quasi-static tension as compared to the dynamic tension. Moreover, under the dynamic tension, the fracture strain of the TR-316L specimens overall showed a slight upward trend with the strain rate. In contrast, the fracture strain of LPBF-316L-BD and LPBF-316L-ND exhibited a slightly decreasing tendency with the strain rate.

4.4.3. Fracture morphology and mode

Fig. 13 present the typical failure modes observed in TR-316L-RD, LPBF-316L-BD and LPBF-316L-ND subjected to quasi-static and dynamic tensile loadings, respectively. As expected, the predominant fracture location for all tested specimens was within the gauge length region. To gain a more profound comprehension of the fracture morphology and mode, SEM observations were conducted on the fracture surfaces of representative specimens, including TR-316L-RD, LPBF-316L-BD and LPBF-316L-ND at two magnification scales of 500 (50 μm) and 2000 (10 μm). These specimens were subjected to three distinct tensile loading rates, including quasi-static, 1 m/s and 8 m/s, and the corresponding results are presented in Fig. 14, Fig. 15 and Fig. 16.

Under such three loading rates, the fracture surfaces of TR-316L-RD featured numerous uneven dimples surrounded by second-phase particles, which were indicative of pronounced ductile failure behaviour [31]. These dimples possessed the capacity to absorb a significant amount of energy, with their size and depth directly impacting the material ductility. Additionally, under the quasi-static tension, as shown in Fig. 14**(a)**, TR-316L-RD exhibited more and smaller dimples when compared to other two dynamic tensile loading conditions, as respectively shown in Fig. 15**(a)** and Fig. 16**(a)**, which collectively contributed to a larger total dimple surface area. This phenomenon helps to explain why TR-316L-RD demonstrated the greater material ductility under the quasi-static tension. In the case of LPBF-316L-BD and LPBF-316L-ND under three different levels of tensile loading rates at the magnification scale of 500 (50 μm), as illustrated in Fig. 14**(b)**, 14**(c)**, 15**(b)**, 15**(c)**, 16**(b)** and 16**(c)**, their fracture surfaces revealed the existence of void defects with varying sizes, which were typical traits of the ductile fracture. As the tensile loading rate increased from quasi-static to 8 m/s, a transition from the predominantly ductile fracture to the combined ductile and brittle fractures was observed. This transition was attributed to the formation of more cleavage faces under the higher tensile loading rate [57,58]. Furthermore, partially unmelted powders were visible at the magnification scale of 2000 (10 μm), and these powders were frequently concealed inside the dimples, indicating the presence of internal defects. These defects tended to cause stress concentration and accelerated the initiation of microcracks that propagated into the macroscopic cracks [32,35]. Also noted in Fig. 14**(c)** at the magnification scale of 2000 (10 μm), continuous large pits were formed, resulting from the detachment of columnar grains [59]. A layered inner morphology was further observed in LPBF-316L-BD in Fig. 16**(b)**. Given that the internal structure of the void was visibly related to the melt pool boundaries, the void defects might originate from substantial residual stresses caused by the fast cooling from the molten state [60], which facilitated the crack formation along the melt pool boundaries, ultimately culminating in fracture and void formation, as illustrated in Fig. 17. The layered inner morphology, aligned parallel to the fracture surface, could be regarded as a crucial factor for distinguishing between the building and normal orientations of LPBF-316L. While this study lacked more reliable microscopic observations to elucidate the corresponding mechanisms, existing literature suggests that the significant differences in strength and ductility between LPBF-316L-BD and LPBF-316L-ND could be attributed to the interlayer bonding and columnar grain orientation. In LPBF-316L-BD, insufficient interlayer bonding under tension caused the lower strength [61,62]. However, owing to the columnar grain-boundary being parallel to the loading direction, and the continuous deflection of cracks during growth increasing the surface friction stress between adjacent columnar grains [38], the crack opening and growth process could be delayed, thus exhibiting the higher ductility. Conversely, in LPBF-316L-ND, where the columnar grain-boundary were perpendicular to the loading direction, the presence of dislocation pile-ups accelerated the formation of microcracks along the columnar grain-boundary [38], resulting in the decreased ductility.

Table 6
Cowper-Symonds model parameters for TR-316L and LPBF-316L.

Specimen	Index	C (s^{-1})	P	Strain rate range (s^{-1})
TR-316L	DIF_y	1891	5.02	0.0016–434.52
	DIF_u	1017,179	4.79	
LPBF-316L	DIF_y	32,615	6.27	0.0019–535.28
	DIF_u	27,027	3.84	

5. . Constitutive model

Owing to the simple structural form and the separate inclusion of strain hardening, strain rate hardening and thermal softening, the Johnson-Cook (J-C) constitutive model [63] has been widely adopted to describe the flow stress of metallic materials under dynamic loading conditions, which is expressed as follows:

$$\sigma_y = \left(A + B\bar{\varepsilon}^{p^n}\right)\left(1 + c\ln\dot{\varepsilon}^*\right)\left(1 - \frac{T - T_r}{T_m - T_r}\right)^m \tag{10}$$

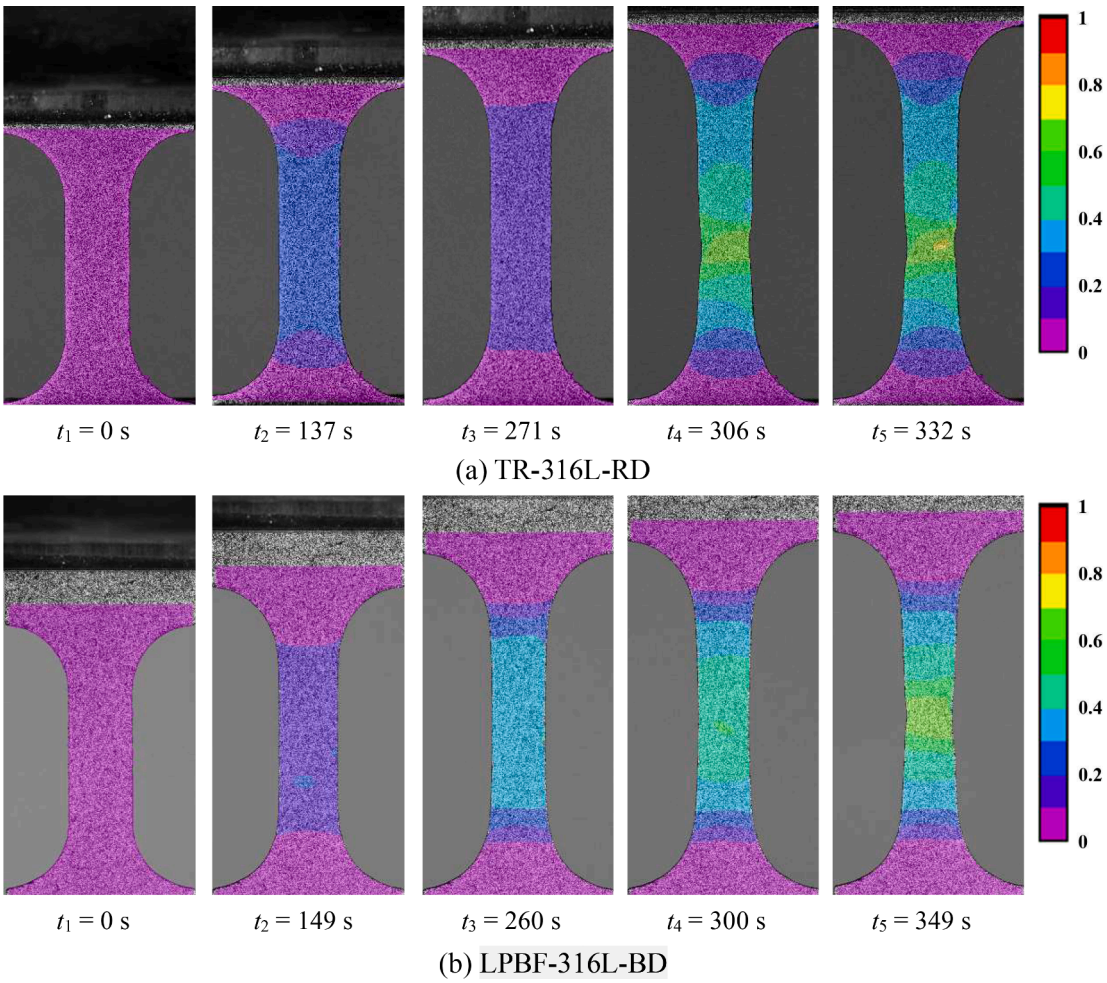

Fig. 10. True strain contours of TR-316L-RD and LPBF-316L-BD under quasi-static tension.

where σ_y denotes the equivalent flow stress; $\bar{\varepsilon}^p$ denotes the equivalent plastic strain; T denotes the present temperature in physical tests; $\dot{\varepsilon}^* = \dot{\varepsilon}/\dot{\varepsilon}_0$ denotes the normalised plastic strain rate, wherein $\dot{\varepsilon}_0$ represents the reference quasi-static strain rate; T_r and T_m represent the room and melt temperatures, respectively; A denotes the yield stress at reference temperature and strain rate (MPa); B represents the strain hardening coefficient (MPa); n signifies the strain hardening exponent; c and m characterise the strain rate and thermal softening coefficients, respectively.

Plastic deformation might result in a temperature rise in the metallic materials [64,65]. When the strain rate is beyond 0.1 s^{-1}, it can be considered an adiabatic condition [66]. In this study, the temperature rises in the rolled and LPBF printed 316L stainless steel specimens during the adiabatic process was estimated using the following equation:

$$\Delta T = \frac{\Delta Q}{\rho C_P} = \frac{\eta}{\rho C_P}\int \sigma d_\varepsilon \tag{11}$$

where ΔT denotes the temperature rise; η denotes the Taylor-Quinney coefficient, which measures the energy converted into heat (ΔQ) and can be typically taken as 0.9 [67]; C_P denotes the specific heat capacity, which was assumed to be 500 J/kg• °C [68]. The integral $\int \sigma d_\varepsilon$ corresponds to the integration of the true plastic stress (σ) with respect to the true plastic strain (ε), which can be obtained from the curves as illustrated in Fig. 18. The temperature rises of the TR-316L and LPBF-316L specimens during dynamic tensile testing were determined and are listed in Table 7. It was found that all the specimens remained below 150 °C considering the room temperature of 25 °C. When the specimen temperature is below 150 °C, the thermal softening effect can be disregarded [69]. Therefore, the influence resulting from the thermal softening on the TR-316L and LPBF-316L specimens was considered negligible in the current study, and the original J-C constitutive model could be simplified as:

$$\sigma_y = \left(A + B\bar{\varepsilon}^{p^n}\right)\left(1 + c\ln\dot{\varepsilon}^*\right) \tag{12}$$

Using the experimental data from the quasi-static and dynamic tensile tests, the model parameters (A, B, c and n) were determined for TR-316L, LPBF-316L-BD and LPBF-316L-ND through the least-square method, which are listed in Table 8. It is important to note that, for TR-316L, which exhibited isotropic behaviour in terms of the material strength (as shown in Fig. 5**(a)** and Fig. 8), the parameter determination did not account for the influence of various rolling directions. In contrast, due to the more noticeable anisotropic behaviour of LPBF-316L, the impact of building direction on its model parameters was considered. The curves, plotted with the fitted values of A, B, c and n in the J-C constitutive model for TR-316L, LPBF-316L-BD and LPBF-316L-ND, are illustrated in Fig. 19**(a)**, Fig. 20**(a)** and Fig. 21**(a)**, respectively. As observed, there was a noticeable disparity between the experimental data and the fitting curves using the J-C constitutive model, especially for the tangent modulus. Thus, modifying the original J-C constitutive model was essential to fairly characterise the flow stress for TR-316L, LPBF-316L-BD and LPBF-316L-ND.

To better represent the strain hardening behaviour of rolled and LPBF printed 316L stainless steels, the Voce hardening model [70] was

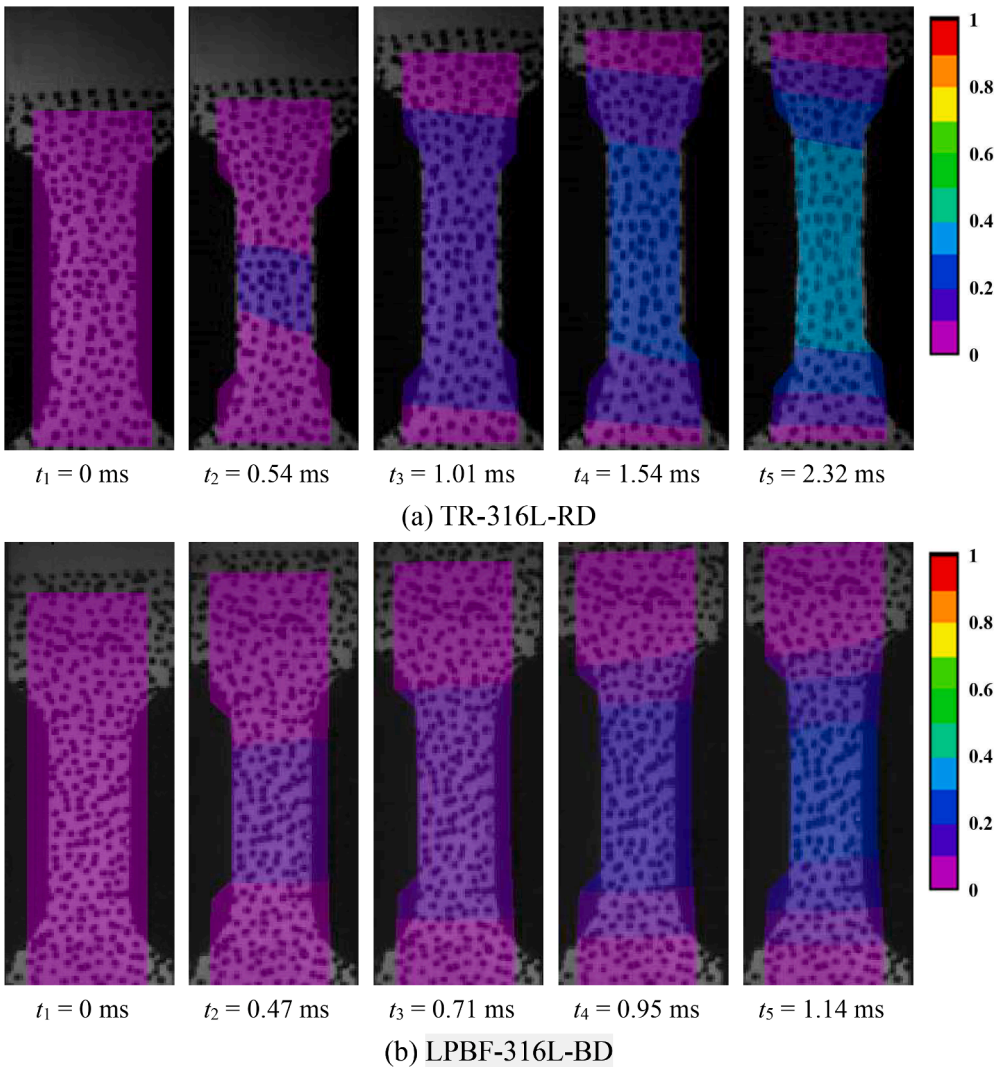

Fig. 11. True strain contours of TR-316L-RD and LPBF-316L-BD at tensile loading rate of 8 m/s.

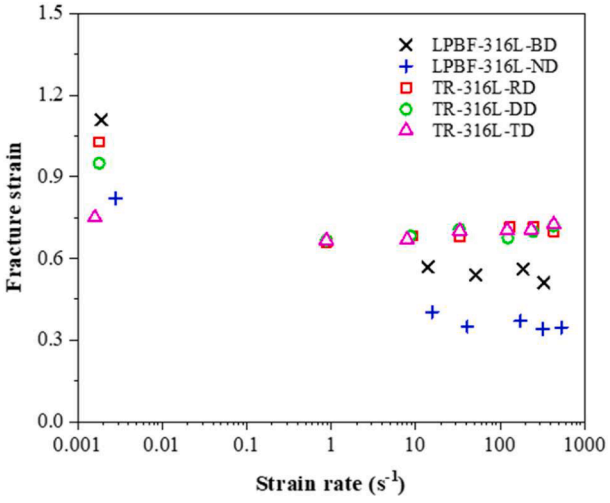

Fig. 12. Actual fracture strains of TR-316L and LPBF-316L specimens versus strain rate.

incorporated in the original J-C constitutive model in the current study. The linearly combined J-C and Voce hardening model is expressed as follows:

$$\sigma_{\mathrm{v}}(\bar{\varepsilon}^{\mathrm{p}}) = A + Q\left(1 - \mathrm{e}^{-\beta\bar{\varepsilon}^{\mathrm{p}}}\right) \tag{13}$$

$$\sigma_{\mathrm{j-v}}(\bar{\varepsilon}^{\mathrm{p}}) = A + \alpha Q\left(1 - \mathrm{e}^{-\beta\bar{\varepsilon}^{\mathrm{p}}}\right) + (1-\alpha)B\bar{\varepsilon}^{\mathrm{p}n} \tag{14}$$

where $\sigma_{\mathrm{v}}(\bar{\varepsilon}^{\mathrm{p}})$ represents the equivalent stress for the Voce hardening model; $\sigma_{\mathrm{j-v}}(\bar{\varepsilon}^{\mathrm{p}})$ represents the equivalent stress for the linearly combined J-C and Voce hardening model; Q and β are material-specific parameters; α is a combination coefficient. Fig. 22 illustrates the correlation between the strain rate sensitivity coefficient c and the equivalent plastic strain $\bar{\varepsilon}^{\mathrm{p}}$ for TR-316L, LPBF-316L-BD and LPBF-316L-ND. As observed, the magnitude of c differed across various strain rates and nonlinearly decreased with $\bar{\varepsilon}^{\mathrm{p}}$. Consequently, an exponential function with respect to $\bar{\varepsilon}^{\mathrm{p}}$ was adopted through the least-square method to improve c, which is given by:

$$c = c_1 + c_2 \times \exp(c_3 \times \bar{\varepsilon}^{\mathrm{p}}) \tag{16}$$

After fitting with the experimental data, the linearly combined J-C and Voce hardening model parameters for TR-316L, LPBF-316L-BD and LPBF-316L-ND are summarised in Table 9. Fig. 19**(b)**, Fig. 20**(b)** and Fig. 21**(b)** respectively depict the stress-strain curves of TR-316L, LPBF-

Fig. 13. Typical failure modes of TR-316L-RD, LPBF-316L-BD and LPBF-316L-ND under quasi-static and dynamic tensile loading conditions.

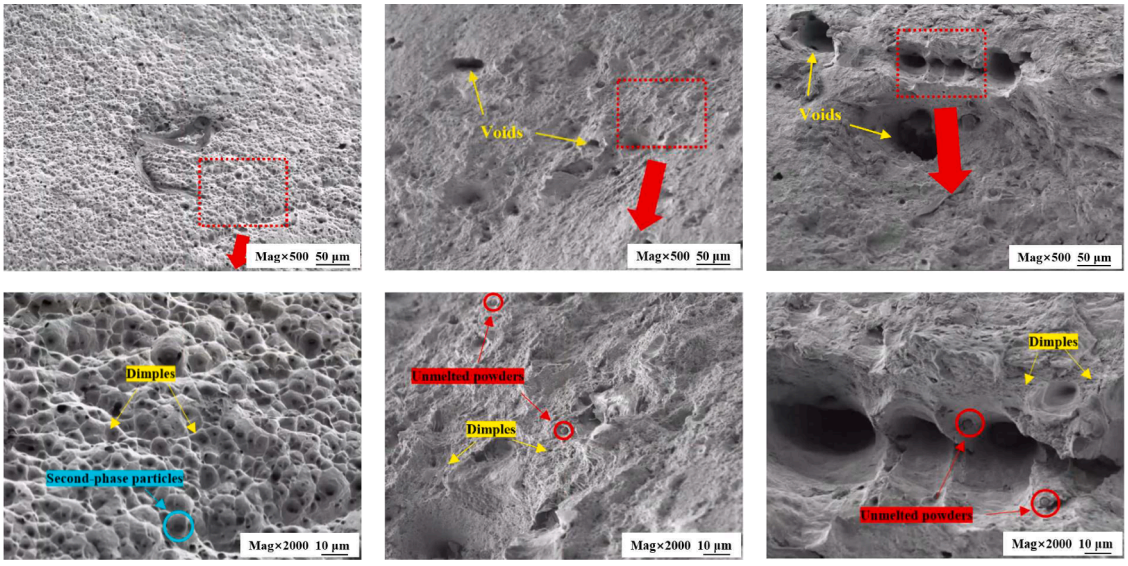

Fig. 14. SEM observations on the fracture surface of TR-316L-RD, LPBF-316L-BD and LPBF-316L-ND under quasi-static tension.

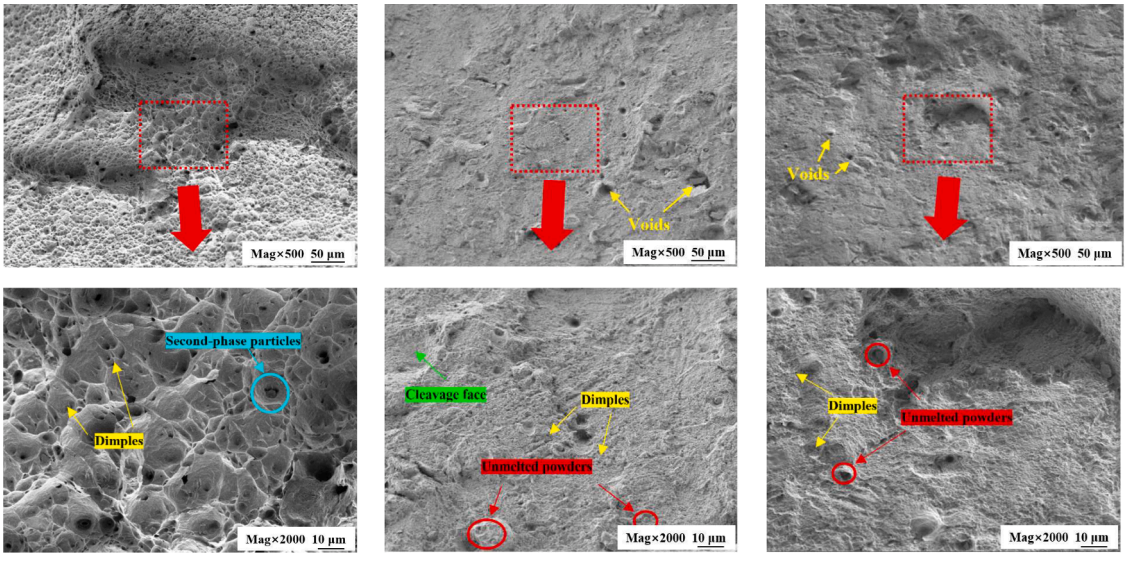

Fig. 15. SEM observations on the fracture surface of TR-316L-RD, LPBF-316L-BD and LPBF-316L-ND at tensile loading rate of 1 m/s.

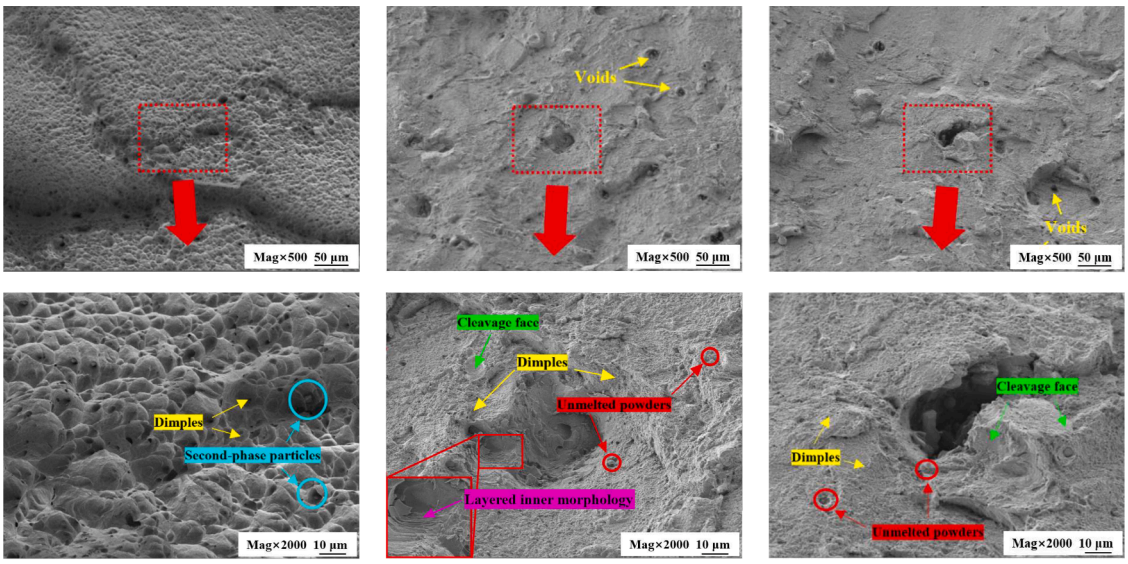

Fig. 16. SEM observations on the fracture surface of TR-316L-RD, LPBF-316L-BD and LPBF-316L-ND at tensile loading rate of 8 m/s.

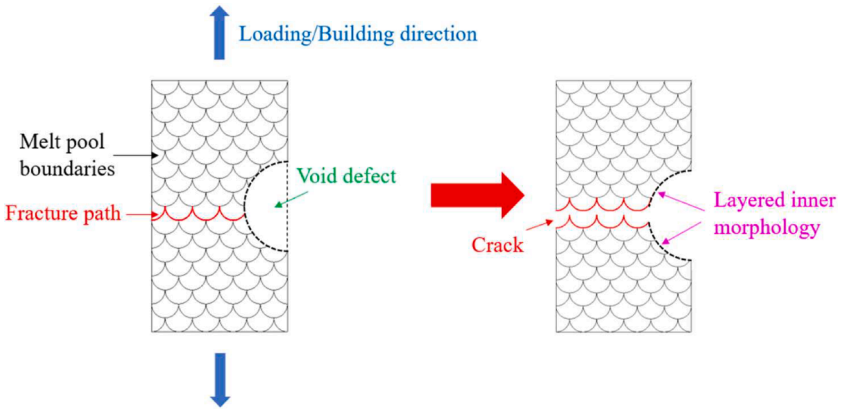

Fig. 17. Fracture path for LPBF-316L-BD under dynamic tension.

316L-BD and LPBF-316L-ND obtained from the modified J-C constitutive model, along with comparisons to the experimental outcomes at different strain rates. The results revealed that the modified J-C constitutive model incorporating the Voce hardening model could more fairly reproduce the flow behaviour of TR-316L, LPBF-316L-BD and LPBF-316L-ND than the original J-C constitutive model.

Although the modified J-C constitutive model, which incorporated the Voce hardening model, could reasonably represent the stress-strain relationship of LPBF-316L-BD and LPBF-316L-ND across a wide range of strain rates, its parameter determination was conducted separately based on various building directions. Therefore, it remains worthwhile to develop a material constitutive model tailored for LPBF-316L in future research endeavours, aiming to predict its dynamic response and failure behaviour in complex loading scenarios. Such a developed model should not only address the coupling between strain rates and building direction-induced anisotropic behaviour but also account for the anisotropic damage evolution [48].

6. Concluding remarks

In this study, physical tests were implemented to comparatively assess both the quasi-static and dynamic tensile behaviours of 316L stainless steel fabricated by traditional rolling and laser-powder bed fusion (LPBF) techniques. Scanning electron microscopy (SEM) was performed to investigate the fracture surfaces of representative specimens and comprehend the fracture morphology and mode. The Cowper-Symonds model was then adopted to determine the strength enhancement of rolled and LPBF printed 316L stainless steels with strain rate. Moreover, a modified Johnson-Cook (J-C) constitutive model incorporating the Voce hardening model and considering the strain rate effect was employed to describe their tensile behaviours. On the basis of the research outcomes, some key conclusions could be deduced herein:

1) Under both quasi-static and dynamic tensile loading conditions, LPBF printed 316L stainless steel displayed a more evident anisotropic behaviour in terms of material strength when compared to rolled 316L stainless steel. Increasing the inclination angle relative to the building direction enhanced the yield and ultimate strengths of LPBF printed 316L stainless steel but led to reduced ductility.
2) LPBF printed 316L stainless steel exhibited greater yield and ultimate strengths in comparison with rolled 316L stainless steel. In contrast, rolled 316L stainless steel demonstrated improved ductility, particularly under dynamic tensile loading conditions.
3) Both rolled and LPBF printed 316L stainless steels displayed positive strain rate sensitivity in terms of material strength, with this sensitivity being more pronounced in yield strength than in ultimate

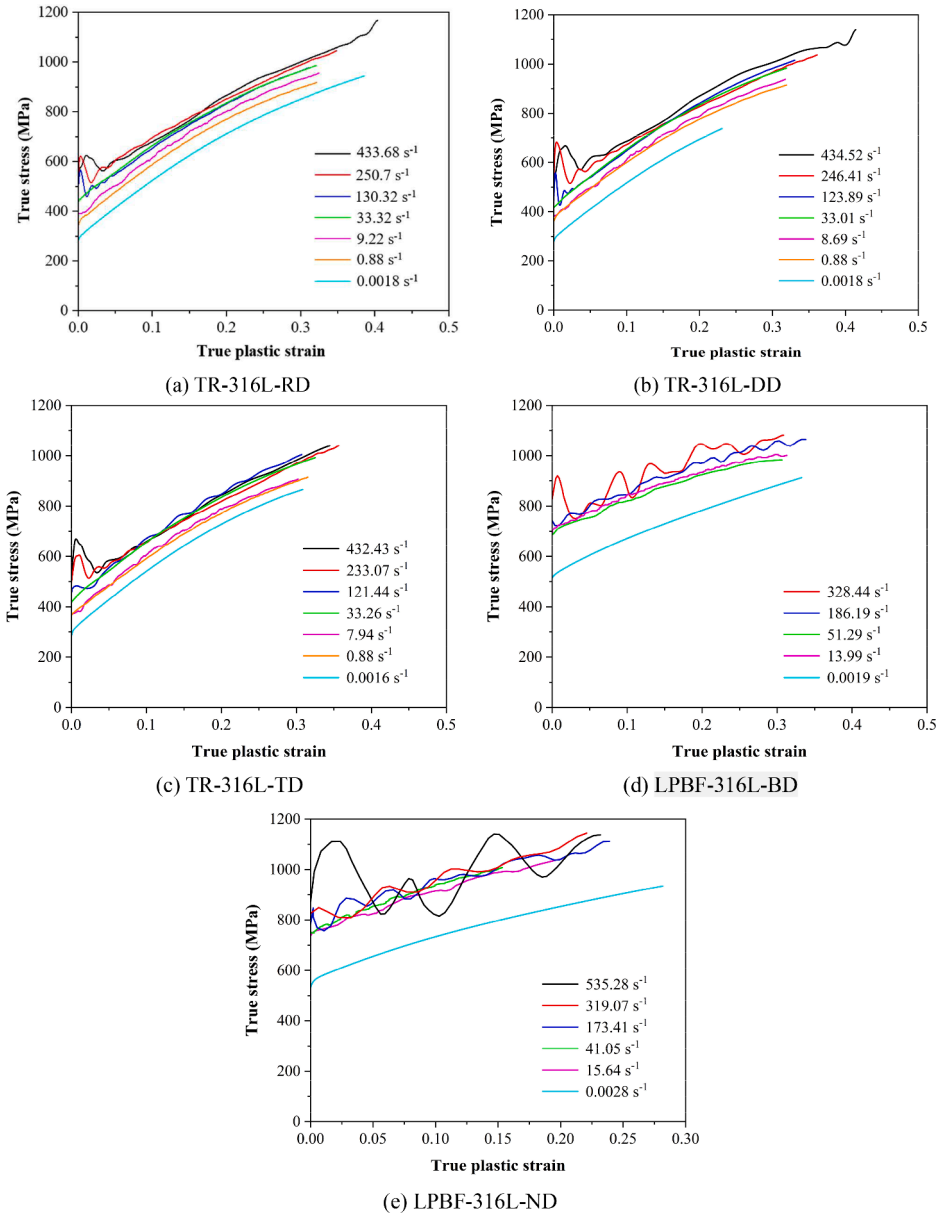

Fig. 18. True plastic stress-strain curves for TR-316L and LPBF-316L specimens.

Table 7
Temperature rise of TR-316L and LPBF-316L specimens (°C).

Specimen	0.03 m/s	0.3 m/s	1 m/s	4 m/s	8 m/s	14 m/s
TR-316L-RD	51.6	54.58	56.91	54.57	65.86	80.78
TR-316L-DD	51.71	53.44	55.99	59.16	67.45	83.7
TR-316L-TD	50.49	48.40	57.51	54.42	65.53	63.9
LPBF-316L-BD	/	60.54	63.03	71.2	66.28	/
LPBF-316L-ND	/	28.78	36.28	50.84	37.66	52.63

'/' means the specimen was not tested in this study.

Table 8
Fitted *A, B, c* and *n* in J-C model for TR-316L, LPBF-316L-BD and LPBF-316L-ND.

Specimen	*A* (MPa)	*B* (MPa)	*c*	*n*
TR-316L	284.89	1401.87	0.017	0.76
LPBF-316L-BD	510.51	929.56	0.023	0.76
LPBF-316L-ND	532.8	950.8	0.027	0.68

strength. LPBF printed 316L stainless steel exhibited lower sensitivity to strain rate in yield strength compared to rolled 316L stainless steel but higher sensitivity in ultimate strength. The strain rate sensitivity of material strengths for LPBF printed 316L stainless steel was independent on the building/loading orientation.

4) Both rolled and LPBF printed 316L stainless steels demonstrated greater actual fracture strains under quasi-static tension compared to dynamic tension. Under dynamic tension, the actual fracture strain of rolled 316L stainless steel overall showed a slight upward trend with strain rate, while LPBF printed 316L stainless steel exhibited a slight reduction in actual fracture strain as the strain rate increased.
5) From SEM observations, the fracture surface of the specimen under quasi-static tension exhibited a larger total dimple surface area induced by more and smaller dimples compared to those under dynamic tension, which contributed to a greater material ductility. As the loading rate increased, a transition from predominantly ductile fracture behaviour to a combination of ductile and brittle fractures occurred due to more cleavage surfaces. When the deposition layers were oriented parallel to the loading direction, interlayer tension

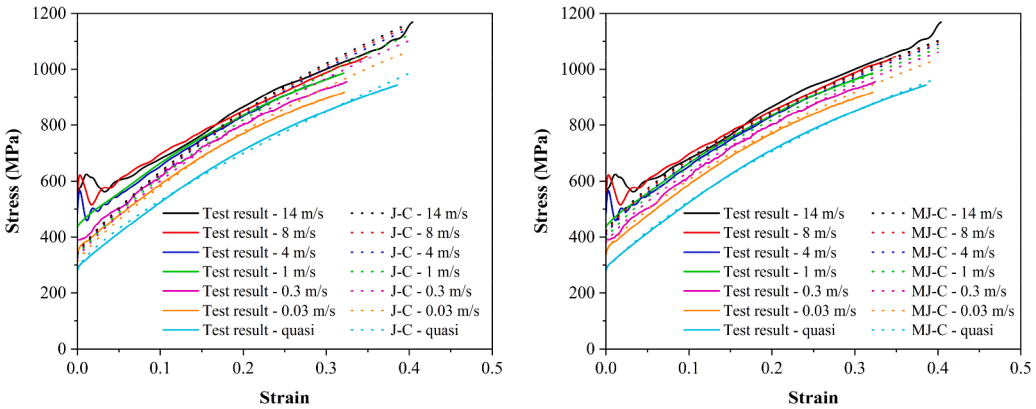

Fig. 19. Comparison between experimental data and proposed constitutive model for TR-316L.

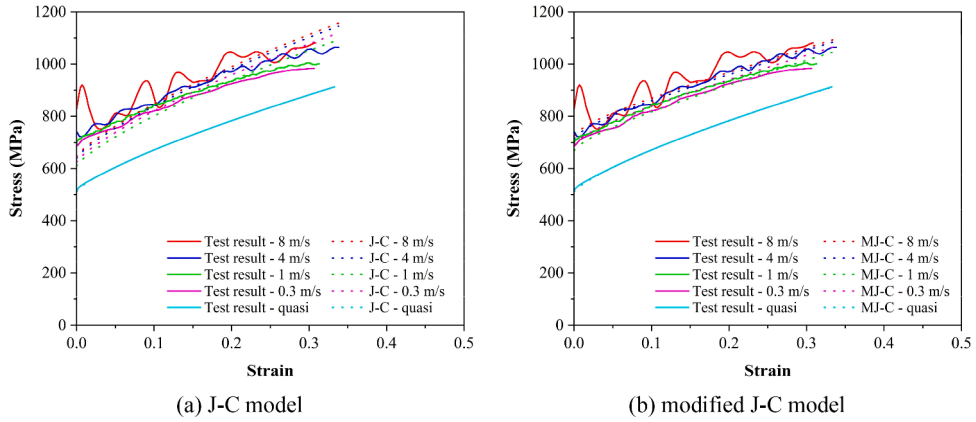

Fig. 20. Comparison between experimental data and proposed constitutive model for LPBF-316L-BD.

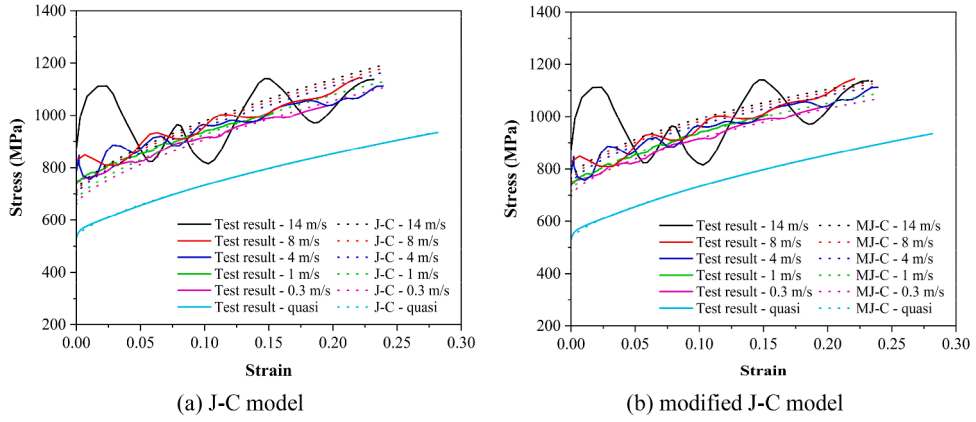

Fig. 21. Comparison between experimental data and proposed constitutive model for LPBF-316L-ND.

could be effectively harnessed to yield higher material strength of LPBF printed 316L stainless steel.

6) The Cowper-Symonds model was fitted based on the experimental data to evaluate the dynamic increase factor (DIF) values of yield and ultimate strengths for rolled and LPBF printed 316L stainless steels. A modified Johnson-Cook (J-C) model that incorporated the Voce hardening model and considered the strain rate effect was fitted using the experimental data to evaluate the flow behaviour of rolled and LPBF printed 316L stainless steels.

The aforementioned research findings elucidate the quasi-static and dynamic mechanical behaviours, as well as the constitutive relationship, of LPBF printed 316L stainless steel influenced by building directions and strain rates. However, it is still essential to note that this study focused solely on the dynamic tensile behaviour of LPBF printed 316L stainless steel in two typical building directions (0 and 90°). To further improve the comprehension of its dynamic tensile behaviour and constitutive relationship affected by additional building directions, future research endeavours could incorporate supplementary experiments to address the limitations of this study. Moreover, for a deeper

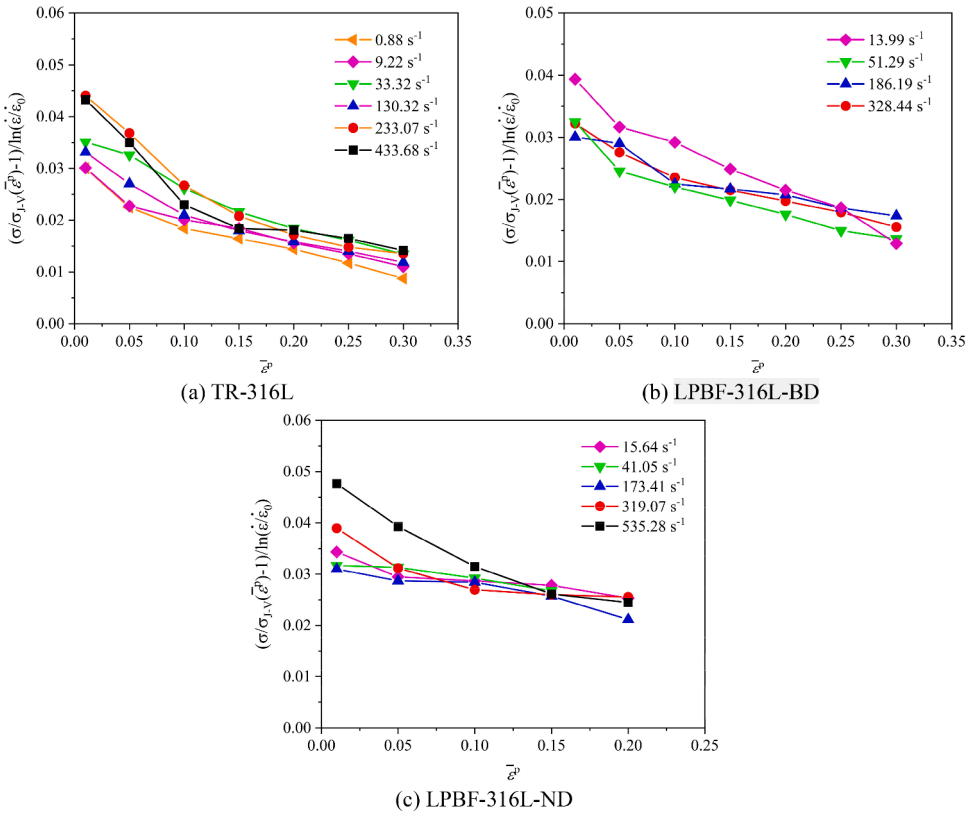

Fig. 22. Correlation between c and $\bar{\varepsilon}^p$ for TR-316L, LPBF-316L-BD and LPBF-316L-ND.

Table 9
J-C and Voce hardening model parameters.

Specimen	α	Q (MPa)	β	c_1	c_2	c_3
TR-316L	0.62	1018.08	2.7	0.01	0.028	−7.35
LPBF-316L-BD	0.15	653.37	2.76	0.015	0.02	−7.02
LPBF-316L-ND	0.08	526.8	4.81	0.009	0.027	−2.71

insight into the fracture mechanism of LPBF printed 316L stainless steel under various strain rates, microstructural observations utilising X-ray or transmission electron microscopy (TEM) techniques at higher magnifications could be employed.

CRediT authorship contribution statement

Jian Liu: Data curation, Funding acquisition, Investigation, Methodology, Writing – original draft, Writing – review & editing. **Le Dong:** Data curation, Investigation, Validation. **Cunyi Li:** Data curation, Investigation, Writing – review & editing. **Jianguang Fang:** Conceptualization, Methodology, Supervision, Writing – review & editing. **Ying Chen:** Funding acquisition, Methodology. **Jian Cui:** Methodology, Project administration.

Declaration of competing interest

The authors declare that they have no known competing financial interests or personal relationships that could have appeared to influence the work reported in this paper.

Data availability

Data will be made available on request.

Acknowledgements

The authors would like to express sincere gratitude for the financial support by the Science and Technology Program of Guangzhou (Grant No. 2024A03J0390) and the National Natural Science Foundation of China (Grant No. 52108446).

References

[1] Attar H, Ehtemam-Haghighi S, Kent D, Dargusch MS. Recent developments and opportunities in additive manufacturing of titanium-based matrix composites: a review. Internat J Mach Tools Manufact 2018;133:85–102.
[2] Azarniya A, Colera XG, Mirzaali MJ, Sovizi S, Bartolomeu F, Wits WW, Yap CY, Ahn J, Miranda G, Silva FS. Additive manufacturing of Ti–6Al–4V parts through laser metal deposition (LMD): process, microstructure, and mechanical properties. J Alloys Compd 2019;804:163–91.
[3] Ding D, Pan Z, Cuiuri D, Li H. Wire-feed additive manufacturing of metal components: technologies, developments and future interests. Internat J Adv Manufact Techn 2015;81:465–81.
[4] Frazier WE. Metal additive manufacturing: a review. J Mater Eng Perform 2014;23:1917–28.
[5] Hmeidat NS, Pack RC, Talley SJ, Moore RB, Compton BG. Mechanical anisotropy in polymer composites produced by material extrusion additive manufacturing. Addit Manuf 2020;34:101385.
[6] Zaiemyekeh Z, Li H, Romanyk DL, Hogan JD. Strain-rate-dependent behavior of additively manufactured alumina ceramics: characterization and mechanical testing. J Mater Res Technol 2024;28:3794–804.
[7] Yang Y, Li L, Zhao J. Mechanical property modeling of photosensitive liquid resin in stereolithography additive manufacturing: bridging degree of cure with tensile strength and hardness. Mater Des 2019;162:418–28.
[8] Bharath C, Shamanth V, Hemanth K. Studies on mechanical behaviour of AlSi10Mg alloy produced by selective laser melting and A360 alloy by die casting. Proceedings 2021;45:78–81.
[9] Zhang L, Shi X, Li N, Zhao L, Chen W. Heterogeneities of microstructure and mechanical properties for inconel 718 strut tensile sample fabricated by selective laser melting. J Mater Res Technol 2021;12:2396–406.
[10] Levy D, Shirizly A, Rittel D. Static and dynamic comprehensive response of additively manufactured discrete patterns of Ti6Al4V. Int J Impact Eng 2018;122:182–96.
[11] Huang J, Qin Q, Wang J. A review of stereolithography: processes and systems. Processes. 2020;8:1138.

[12] Khorasani A, Gibson I, Veetil JK, Ghasemi AH. A review of technological improvements in laser-based powder bed fusion of metal printers. Internat J Adv Manufact Techn 2020;108:191–209.
[13] Kristoffersen M, Costas M, Koenis T, Brøtan V, Paulsen CO, Børvik T. On the ballistic perforation resistance of additive manufactured AlSi10Mg aluminium plates. Int J Impact Eng 2020;137:103476.
[14] Olakanmi EO, Cochrane RF, Dalgarno KW. A review on selective laser sintering/melting (SLS/SLM) of aluminium alloy powders: processing, microstructure, and properties. Prog Mater Sci 2015;74:401–77.
[15] ISO/ASTM 52900. Additive manufacturing—general principles—fundamentals and vocabulary 2021.
[16] 35351-2017 GT. Additive manufacturing-Terminology. Beijing: China Standard Press; 2017 (In Chinese).
[17] Meiners W, Wissenbach K, Gasser A. Shaped body especially prototype or replacement part production. DE Patent 1998:19.
[18] Afkhami S, Javaheri V, Dabiri E, Piili H, Björk T. Effects of manufacturing parameters, heat treatment, and machining on the physical and mechanical properties of 13Cr10Ni1· 7Mo2Al0· 4Mn0· 4Si steel processed by laser powder bed fusion. Mater Sci Eng 2022;832:142402.
[19] Yin Y, Sun J, Guo J, Kan X, Yang D. Mechanism of high yield strength and yield ratio of 316L stainless steel by additive manufacturing. Mater Sci Eng 2019;744:773–7.
[20] Bedmar J, Abu-Warda N, García-Rodríguez S, Torres B, Rams J. Influence of the surface state on the corrosion behavior of the 316L stainless steel manufactured by laser powder bed fusion. Corros Sci 2022;207:110550.
[21] Kale AB, Singh J, Kim BK, Kim D-I, Choi SH. Effect of initial microstructure on the deformation heterogeneities of 316L stainless steels fabricated by selective laser melting processing. J Mater Res Technol 2020;9:8867–83.
[22] Hukpati K, Eliasu A, Tetteh F, Czekanski A, Boakye-Yiadom S. Effect of printing parameters on the structure and high strain rate deformation behavior of additively manufactured 316L stainless steel. Mater Sci Eng 2022;853:143710.
[23] Ahmadi A, Mirzaeifar R, Moghaddam NS, Turabi AS, Karaca HE, Elahinia M. Effect of manufacturing parameters on mechanical properties of 316L stainless steel parts fabricated by selective laser melting: a computational framework. Mater Des 2016;112:328–38.
[24] Branch BA, Specht PE, Jensen S, Jared B. Detailed meso-scale simulations of the transient deformation in additively manufactured 316L stainless steel lattices characterized by phase contrast imaging. Int J Impact Eng 2022;161:104112.
[25] Gray III GT, V Livescu, P Rigg, CP Trujillo, CM Cady, S-R Chen, JS Carpenter, TJ Lienert, SJ Fensin. Structure/property (constitutive and spallation response) of additively manufactured 316L stainless steel. Acta Mater 2017;138:140–9.
[26] Güden M, Enser S, Bayhan M, Taşdemirci A, Yavaş H. The strain rate sensitive flow stresses and constitutive equations of a selective-laser-melt and an annealed-rolled 316L stainless steel: a comparative study. Mater Sci Eng 2022;838:142743.
[27] Li X, Roth CC, Tancogne-Dejean T, Mohr D. Rate-and temperature-dependent plasticity of additively manufactured stainless steel 316L: characterization, modeling and application to crushing of shell-lattices. Int J Impact Eng 2020;145:103671.
[28] Xue H, Wang T, Cui X-y, Wang Y-f, Huang G-y. On the ballistic perforation performance of additively manufactured 316L stainless steel cylindrical projectiles. Int J Impact Eng 2023;178:104625.
[29] Yu H, Chen R, Liu W, Li S, Chen L, Hou S. Dynamic mechanical behavior and microstructural evolution of additively manufactured 316L stainless steel. J Mater Sci 2022;57:8425–41.
[30] Piao M, Huh H, Lee I, Ahn K, Kim H, Park L. Characterization of flow stress at ultra-high strain rates by proper extrapolation with Taylor impact tests. Int J Impact Eng 2016;91:142–57.
[31] Khodabakhshi F, Farshidianfar M, Gerlich A, Nosko M, Trembošová V, Microstructure Khajepour A. strain-rate sensitivity, work hardening, and fracture behavior of laser additive manufactured austenitic and martensitic stainless steel structures. Mater Sci Eng 2019;756:545–61.
[32] Li Z, Voisin T, McKeown JT, Ye J, Braun T, Kamath C, King WE, Wang YM. Tensile properties, strain rate sensitivity, and activation volume of additively manufactured 316L stainless steels. Int J Plast 2019;120:395–410.
[33] Jiang HZ, Li ZY, Feng T, Wu PY, Chen QS, Yao SK, Hou JY. Effect of annealing temperature and strain rate on mechanical property of a selective laser melted 316L stainless steel. Acta Metallurgica Sinica (English Letters) 2022;35:773–89.
[34] Tancogne-Dejean T, Roth CC, Mohr D. Rate-dependent strength and ductility of binder jetting 3D-printed stainless steel 316L: experiments and modeling. Int J Mech Sci 2021;207:106647.
[35] Carassus H, Guérin J, Morvan H, Haugou G, Sadat T, Guérard S, Markiewicz E. An experimental investigation into influences of build orientation and specimen thickness on quasi-static and dynamic mechanical responses of Selective Laser Melting 316L Stainless Steel. Mater Sci Eng 2022;835:142683.
[36] Güden M, Yavaş H, Tanrıkulu AA, Taşdemirci A, Akın B, Enser S, Karakuş A, Hamat BA. Orientation dependent tensile properties of a selective-laser-melt 316L stainless steel. Mater Sci Eng 2021;824:141808.
[37] Carroll BE, Palmer TA, Beese AM. Anisotropic tensile behavior of Ti–6Al–4V components fabricated with directed energy deposition additive manufacturing. Acta Mater 2015;87:309–20.
[38] Ni M, Chen C, Wang X, Wang P, Li R, Zhang X, Zhou K. Anisotropic tensile behavior of in situ precipitation strengthened Inconel 718 fabricated by additive manufacturing. Mater Sci Eng 2017;701:344–51.
[39] Niendorf T, Leuders S, Riemer A, Richard HA, Tröster T, Schwarze D. Highly anisotropic steel processed by selective laser melting. Metallurg Mater Transact B 2013;44:794–6.
[40] Alaghmandfard R, Chalasani D, Hadadzadeh A, Amirkhiz BS, Odeshi A, Mohammadi M. Dynamic compressive response of electron beam melted Ti–6Al–4V under elevated strain rates: microstructure and constitutive models. Addit Manuf 2020;35:101347.
[41] Yuan Y, Zhang Y, Qiao Y, Xie J, Xu Q, Qi Y, Zhang W, Chen P. Effect of build orientation on dynamic compressive behaviour of Ti-6Al-4V alloy fabricated by selective laser melting. Materi Sci Eng 2023;862:144440.
[42] Chen W, Hao H, Jong M, Cui J, Shi Y, Chen L, Pham TM. Quasi-static and dynamic tensile properties of basalt fibre reinforced polymer. Composites Part B 2017;125:123–33.
[43] Boyce BL, Dilmore MF. The dynamic tensile behavior of tough, ultrahigh-strength steels at strain-rates from 0.0002 s^{-1} to 200 s^{-1}. Int J Impact Eng 2009;36:263–71.
[44] Chen W, Hao H, Hughes D, Shi Y, Cui J, Li ZX. Static and dynamic mechanical properties of expanded polystyrene. Mater Des 2015;69:170–80.
[45] Li ZX, Zhang X, Shi Y. Experimental study on dynamic properties of BFRP laminates used for structural strengthening under high strain rates. Constr Build Mater 2020;251:118731.
[46] Chen Y, Hao H, Chen W, Cui J, Hao Y, Hua C. Dynamic tensile behaviors of welded steel joint material. J Constr Steel Res 2021;183:106700.
[47] Kim JK, Kwon MH, De Cooman BC. On the deformation twinning mechanisms in twinning-induced plasticity steel. Acta Mater 2017;141:444–55.
[48] Li C, Fang J, Wan Y, Qiu N, Steven G, Li Q. Phase field fracture model for additively manufactured metallic materials. Int J Mech Sci 2023;251:108324.
[49] Sun M, Packer JA. High strain rate behaviour of cold-formed rectangular hollow sections. Eng Struct 2014;62:181–92.
[50] Malvar LJ. Review of static and dynamic properties of steel reinforcing bars. Mater J 1998;95:609–16.
[51] Malvar LJ, Crawford JE. Dynamic increase factors for concrete. DTIC Doc 1998;1:1.6.
[52] Cowper G.R., Symonds P.S. Strain-hardening and strain-rate effects in the impact loading of cantilever beams. 1957.
[53] Bardelcik A, Worswick M, Winkler S, Wells M. A strain rate sensitive constitutive model for quenched boron steel with tailored properties. Int J Impact Eng 2012;50:49–62.
[54] Liu J, Li J, Fang J, Liu K, Su Y, Wu C. Investigation of ultra-high performance concrete slabs under contact explosions with a calibrated K&C model. Eng Struct 2022;255:113958.
[55] Liu J, Wu C, Li J, Su Y, Shao R, Liu Z, Chen G. Experimental and numerical study of reactive powder concrete reinforced with steel wire mesh against projectile penetration. Int J Impact Eng 2017;109:131–49.
[56] Rohr I, Nahme H, Thoma K. Material characterization and constitutive modelling of ductile high strength steel for a wide range of strain rates. Int J Impact Eng 2005;31:401–33.
[57] Cruz V, Qiu Y, Birbilis N, Thomas S. Stress corrosion cracking of 316L manufactured by laser powder bed fusion in 6% ferric chloride solution. Corros Sci 2022;207:110535.
[58] Jiang Q, Li S, Guo S, Fu M, Zhang B. Comparative study on process-structure-property relationships of TiC/Ti6Al4V and Ti6Al4V by selective laser melting. Int J Mech Sci 2023;241:107963.
[59] Wang C, Tan X, Liu E, Tor SB. Process parameter optimization and mechanical properties for additively manufactured stainless steel 316L parts by selective electron beam melting. Mater Des 2018;147:157–66.
[60] Liverani E, Toschi S, Ceschini L, Fortunato A. Effect of selective laser melting (SLM) process parameters on microstructure and mechanical properties of 316L austenitic stainless steel. J Mater Process Technol 2017;249:255–63.
[61] Guo P, Zou B, Huang C, Gao H. Study on microstructure, mechanical properties and machinability of efficiently additive manufactured AISI 316L stainless steel by high-power direct laser deposition. J Mater Process Technol 2017;240:12–22.
[62] Narasimharaju SR, Zeng W, See TL, Zhu Z, Scott P, Jiang X, Lou S. A comprehensive review on laser powder bed fusion of steels: processing, microstructure, defects and control methods, mechanical properties, current challenges and future trends. J Manuf Process 2022;75:375–414.
[63] Jonhson G, Cook W. A constitutive model and data for metal subjected to large strains, high strain rates and high temperature. In: Proceedings of the Seventh International Symposium on Ballistic; 1983. p. 19–21.
[64] Hansen N, Barlow C. Plastic deformation of metals and alloys. Physical Metallurgy: Elsevier; 2014. p. 1681–764.
[65] Kapoor R. Nemat-Nasser S. Determination of temperature rise during high strain rate deformation. MechMater 1998;27:1–12.
[66] Dixit S, Liu S, Murdoch HA, Smith PM. Investigating build orientation-induced mechanical anisotropy in additive manufacturing 316L stainless steel. Mater Sci Eng 2023:145308.
[67] Rittel D, Zhang L, Osovski S. The dependence of the Taylor–Quinney coefficient on the dynamic loading mode. J Mech Phys Solids 2017;107:96–114.
[68] Samuel K, Mannan S, Radhakrishnan V. The influence of temperature and prior cold work on the strain-hardening parameters of a type 316 LN stainless steel. Internat J Press Vessels Pip 1992;52:151–7.
[69] Chen J, Young B, Uy B. Behavior of high strength structural steel at elevated temperatures. J Struct Eng 2006;132:1948–54.
[70] Voce E. The relationship between stress and strain for homogeneous deformation. J Institute Metals 1948;74:537–62.